



HAL
open science

Simulation and data processing techniques to design optimized PPR systems on plasma fusion devices

E. Ricardo, F. da Silva, Stéphane Heuraux, A. Silva, J. Santos

► **To cite this version:**

E. Ricardo, F. da Silva, Stéphane Heuraux, A. Silva, J. Santos. Simulation and data processing techniques to design optimized PPR systems on plasma fusion devices. *Computer Physics Communications*, 2024, 294, pp.108945. 10.1016/j.cpc.2023.108945 . hal-04237328

HAL Id: hal-04237328

<https://hal.univ-lorraine.fr/hal-04237328>

Submitted on 11 Oct 2023

HAL is a multi-disciplinary open access archive for the deposit and dissemination of scientific research documents, whether they are published or not. The documents may come from teaching and research institutions in France or abroad, or from public or private research centers.

L'archive ouverte pluridisciplinaire **HAL**, est destinée au dépôt et à la diffusion de documents scientifiques de niveau recherche, publiés ou non, émanant des établissements d'enseignement et de recherche français ou étrangers, des laboratoires publics ou privés.

Simulation and data processing techniques to design optimized PPR systems on plasma fusion devices

E. Ricardo^a, F. da Silva^a, S. Heurax^b, A. Silva^a, J. Santos^a

^a*Instituto de Plasmas e Fusão Nuclear, Instituto Superior Técnico, Av. Rovisco Pais, no. 1, Lisbon, Portugal*

^b*Institut Jean Lamour UMR 7198 CNRS-Université de Lorraine, ARTEM BP 50840, Nancy F-54011, France*

A B S T R A C T

Plasma position reflectometry (PPR) will be used for measuring the plasma position and shape in DEMO. To ensure the reliability, PPR systems are optimized for the expected range of plasmas foreseen during the operation. The study and optimization of PPR systems is a highly demanding computational task and the current approach to define the simulation setup is time-consuming and does not allow the study of a large number of configurations in useful time.

In this article we automate the simulation process required for studying and optimizing PPR systems with the REFMUL family of full-wave FDTD codes. A general overview of the fundamental concepts of PPR systems is presented in the context of reflectometry simulations. Different solutions are proposed to produce realistic reflectometer models from CAD files, realistic plasma models, minimize the complexity of the input definition, manage the simulations in HPCs and analyze the simulation results of PPR systems. A new algorithm based in the In-phase and Quadrature (I/Q) detection scheme is developed to extract the phase derivative and the detected signal amplitude from the synthetic signals of a generic simulation. These techniques allow a brute-force approach to reflectometry problems, being essential for the study of reflectometry systems. The algorithms are validated using the 2017 DEMO baseline scenario to test more than 100 different reflectometers at different poloidal positions in the same toroidal section. The application of our methodology can be extended to different reflectometry techniques and other fields.

1. Introduction

Microwave reflectometry has been used to measure electron density profiles and study turbulent fluctuations in fusion experiments [1, 2, 3]. Fast sweeping reflectometry systems measure the edge electron density profile evolution in a very short time scale, below the fastest time scale associated to MHD events and turbulence [4, 5]. A reflectometry-based plasma position control system was recently demonstrated in real-time in the equatorial region of ASDEX Upgrade [5, 6, 7]. With the knowledge of the edge density profile that is directly linked to the magnetic flux surfaces, it is possible to estimate the separatrix position. This technique, known as plasma position reflectometry (PPR), was proposed as an alternative method to complement or substitute the magnetic diagnostics in DEMO to provide the plasma position and shape [8]. Microwave reflectometry is known for its reduced access, robustness and reliability, fulfilling the requirements to the operation in a fusion reactor with the necessary spatial (<1 cm) and temporal (~ 1 - 10 μ s) resolution. The only in-vessel components are the antennas facing the plasma used to emit and detect the probing beam, the waveguides and the cooling systems, easily adapted to the available space [9, 10, 11].

The DEMO plasma position reflectometer (DEMO PPR) will be composed of multiple O-mode reflectometers distributed poloidally along the DEMO wall, implemented with the slim cassette concept [12]. The separatrix shape will be determined by applying a reconstruction method to the separatrix position measurements from the different locations [13]. This system is in the early development stage and many questions related with the measurement error and its stability need to be investigated before it reaches its final design. The design of a PPR system involves identifying a set of N_R reflectometers positioned at different locations and arranged in a specific geometric configuration that fulfills the imposed constraints while optimizing the measurements. The constraints are divided into seven types. The physical constraints (i) consist in the expected range of plasma configurations for which the PPR system will work, determining the frequency range to be used. It includes the definition of the density profile associated to the equilibrium scenario, the transient states and the perturbations that may occur during the discharge, including the limiting cases. It also takes into account the definition of the temperature profile if the relativistic effects [14] are important and of the magnetic field if the system works with X mode. The geometry constraints (ii) define the available space for the implementation of the reflectometers. They depend on the wall geometry, the location of the ports, blankets geometry, thermal protections and of the geometry of other in-vessel elements. The thermomechanical constraints (iii) define the temperature and stress limits of the system mechanical structure. The control system constraints (iv) define the minimum/ideal number of measurements, its position and the limits of position error (minimum and maximum error, rate of failure) [13]. The hardware constraints (v) impose the physical limits on the sweeping rate, determine the measurement duration, the resolution and the minimum detection power (e.g. ADC sampling frequency, microwave sources). The computational constraints (vi) impose limitations on the maximum number of configurations that can be simulated during its design. Since the project of a PPR system has a pre-defined duration (vii), a strategy of selection of configurations must be applied, allowing to find the solution in the available time.

In general, the design of a PPR system is an iterative process that involves different teams working together in five different tasks: (i) the design of the reflectometer mechanical structure, (ii) the analysis of the thermomechanical properties of a given system configuration under the expected fusion conditions, (iii) the design and analysis of the power losses of the in-vessel systems (waveguides, antennas), (iv) the evaluation of the reflectometer measurement performance (plasma position error and power losses between the emission and detection) and (v) the design of the reflectometer hardware (microwave sources, detector, microwave circuit, waveguides, antennas) and software (data processing, supervision, regulation). An initial reference configuration that fulfills the thermomechanical and spatial constraints is tested and optimized to the expected range of plasma parameters. This process requires the numerical simulation of the measurement process and the estimation of the position error and of the detected power of multiple reflectometers, with different geometry configurations, and for different plasma scenarios. This is in general a very demanding and time-consuming computational task and the current approach of simulation setup definition and data analysis methods do not allow the study of a large number of configurations in the available time.

The simulation of fast sweeping reflectometry systems requires: a (i) wide frequency bandwidth (18-160 GHz), (ii) time-varying probing frequency (sweeping frequency rate from 10 to 100 GHz/ μ s), and (iii) the possibility of fast time evolution of the plasma properties. The Finite-Differences Time-Domain (FDTD) method based on Yee's scheme has been widely adopted to study the performance of reflectometry systems due to its versatility. The REFMUL family of full-wave FDTD codes have been used successfully to realize studies in ASDEX Upgrade, Tore Supra [15], ITER [16], and for assessing microwave diagnostics for DEMO [17]. The simulation dimension is chosen based on the phenomena under study, available computational resources and project duration [18, 19]. One-dimensional simulations

consider various one-dimensional plasma effects but do not include the description of the antenna setup, and power decrease due to the beam geometry is ignored. They are computationally efficient for the most applications. Two-dimensional simulations include both reflectometer geometry and the plasma models in two dimensions, accounting for effects as the poloidal plasma density gradient or the radiation pattern of the probing beam. Two-dimensional simulations require more computational resources but provide a more accurate determination of the phase-shift and power losses can be estimated unlike in one-dimensional simulations. Three dimensional simulations provide a realistic description of both the reflectometer geometry and of the plasma. They calculate all the components of Maxwell's equations, allowing a realistic estimation of the detected signal amplitude. However, running these simulations requires the use of HPCs. Currently, the best solution to optimize PPR systems in tokamaks is the two-dimensional codes. These codes combine several effects of the reflectometer geometry and plasma while requiring acceptable computational resources for multiple simulations. Many effects that contribute to the perturbation of the round-trip time-delay are well described in the poloidal cross-section. Although the detected amplitude in two-dimensional simulations does not represent realistic values, an increase in the 3D detected amplitude is expected to correspond to an increase of the 2D detected amplitude, leading to the same optimized solution. The optimized solution can then be tested with 3D simulations on a reduced set of plasma scenarios to rescale the 2D results.

This article presents an automated approach for studying PPR systems, covering the process from the input definition to the data analysis for a general input configuration. Several aspects related with reflectometry simulation and the study of PPR systems are discussed, proposing different solutions to create realistic plasma/reflectometer models and simplify the input definition. The developed techniques allow for a brute-force approach to reflectometry problems and can be used to optimize a generic PPR system for the equilibrium scenario and evaluate its performance during the discharge. In section 2 we present a general overview of the fundamental concepts of plasma position reflectometry systems. We review the conventional reflectometry model and the detection schemes in the context of reflectometry simulation. The principal techniques for extracting group delay and the signal amplitude from the detected signals are discussed. The position error and the detected signal amplitude are defined and the error sources are analyzed. We generalize the study of reflectometry systems introducing the concept of multi-reflectometer system (MRS), which is valid regardless the reflectometry technique. The system variables are labeled with indices, their dependencies are analyzed and the data processing of a PPR system is generalized. In section 3, we propose a framework structure to simplify the simulation process for a set of independent multi-reflectometer systems. We demonstrate that all the variables involved in simulating MRSs with FDTD codes of different dimensions can be expressed as functions of a reduced number of main variables. These main variables represent groups of independent input variables. This approach enables the definition of inputs using independent lists of variables and a list of dependencies that simulation scripts rely on, ultimately simplifying and generalizing all the simulation process. In Section 4, we discuss the automation of data analysis for PPR systems. We introduce a new algorithm based on I/Q detection for obtaining the position error and detected signal amplitude. To validate these techniques, we test a system of 100 reflectometers, utilizing the 2017 DEMO baseline scenario available in the official EUROfusion database [20]. The results are compared with the manual data analysis. Finally, we present the conclusions in Section 5.

2. Plasma position reflectometry systems

2.1. The basics of plasma position reflectometry

The theoretical model for electron density profile measurement considers a plane wave of frequency f propagating in a slow varying one-dimensional frozen cold plasma, being mostly reflected in a linear plasma permittivity profile. The phase-shift associated to the round trip [1, 21, 22], also mentioned as WKB phase, is given by

$$\varphi(f) = \frac{4\pi}{c} f \int_{x_p}^{x_c(f)} N(x, f) dx - \frac{\pi}{2}, \quad (1)$$

where x_p is the initial plasma position, x_c the cutoff position, and $N(x, f)$ the refractive index, dependent on the propagation mode. The group delay $\tau_g(f)$ is proportional to the derivative of $\varphi(f)$,

$$\tau_g(f) = 2 \int_{x_p}^{x_c(f)} \frac{1}{v_g(x)} dx = \frac{2}{c} \int_{x_p}^{x_c(f)} \frac{\partial}{\partial f} [fN(x, f)] dx = \frac{1}{2\pi} \frac{\partial \varphi}{\partial f}, \quad (2)$$

where v_g is the group velocity. For O-mode propagation ($\mathbf{k} \perp \mathbf{B}_0$) the cutoff frequency f_c occurs at the plasma frequency, $f_c = f_p$. The cutoff electron density n_c is proportional to the square of the probing frequency F , given by the equation:

$$n_c(F) = n_e(x_c) = 4\pi^2 \frac{\epsilon_0 m_e}{e^2} F^2 = \frac{F^2}{\alpha_0} \simeq \frac{(F[\text{Hz}])^2}{80.6164} \text{ [m}^{-3}\text{]}. \quad (3)$$

In this case, the cutoff position x_c associated with a given probing frequency F can be directly calculated with the Abel inversion method for a monotonic density profile [1, 21]:

$$x_c(F) = x_p + \frac{c}{2\pi^2} \int_0^F \frac{d\varphi}{df} \frac{1}{\sqrt{F^2 - f^2}} df = x_p + \frac{c}{\pi} \int_0^F \frac{\tau(f)}{\sqrt{F^2 - f^2}} df. \quad (4)$$

If $\tau(f)$ is defined in the $0 - F_{max}$ range, the density profile $[x_c(F), n(F)]$ is reconstructed from $n_{min} = 0$ to $n_{max} = \alpha_0^{-1} F_{max}^2$. The analytical inversion of the X mode is not possible due to its complicated dispersion relation and a numerical method needs to be implemented to reconstruct the density profile [23]. In plasma position reflectometry, the position is determined with the knowledge of the separatrix density provided by other diagnostic [5] or obtained directly through profile shape analysis. The O-mode is preferred due to the fact the profile reconstruction is independent from the magnetic field. A position reflectometer consists technically of a conventional fast sweeping reflectometer, with some differences in the data processing software. By measuring at different locations of the machine, it is possible to reconstruct the separatrix shape with a reconstruction algorithm [13].

2.2. The reflectometer set-up and detection schemes

A generic reflectometer is composed of microwave sources, transmission lines, antennas, detectors and the hardware for data analysis. Reflectometers, similarly to a radar systems, can be categorized as mono-static, bi-static or multi-static, depending on the number of antennas involved in the measurement. In a mono-static reflectometer, the emitting antenna is also used to signal detecting. Bi-static systems use separate antennas for emission and detection while multi-static reflectometers involve multiple antennas for signal detection. Some systems may feature multiple emitting antennas operating in different bands. Mono-static configurations offer advantages over the bi/multi-static arrangements as they optimize signal reflection for ideal plasma conditions while minimizing the space required for emission and reception. Hence, in principle, mono-static reflectometers are preferred for fusion reactor applications. If achieving the ideal plasma condition is not possible, solutions may involve optimizing the angle of emission. The hardware techniques and the specifications of the microwave circuits used in reflectometry are beyond the scope of this work, as there is literature on the subject [22, 24]. However, a brief review of the principles of homodyne/in-phase and quadrature detection schemes is necessary in the context of the simulation of PPR systems as they are part of the automation process. The scheme of a homodyne reflectometer setup for phase detection is shown in figure 1 (a) and the In-phase and Quadrature (IQ) detection setup in figure 1 (b), both with a bi-static configuration.

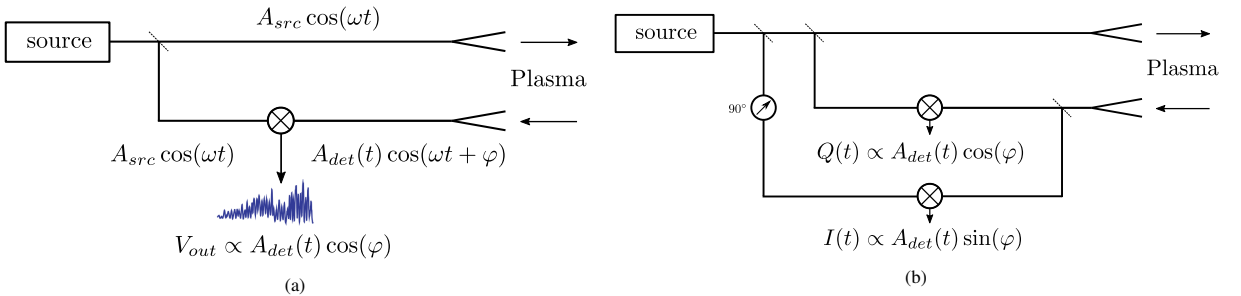


Fig. 1: (a) Bi-static homodyne detection scheme. Adapted from [25]. (b) IQ detection scheme.

In the homodyne setup the reference signal from the source,

$$S_{src}(t) = A_{src}(t) \cos[\omega t], \quad (5)$$

is mixed with the reflected signal from the plasma that contains information on the phase shift and amplitude,

$$S_{det}(t) = A_{det}(t) \cos[\omega t + \varphi(t)]. \quad (6)$$

The mixed signal is composed of a low and high frequency component:

$$S_{mix}(t) = S_{src}(t)S_{det}(t) = \frac{1}{2}A_{src}(t)A_{det}(t) \cos[\varphi] + \frac{1}{2}A_{src}(t)A_{det}(t) \cos[2\omega t + \varphi(t)]. \quad (7)$$

By applying a low-pass filter (LPF) in the mixed signal, a component proportional to $\cos[\varphi(t)]$ is obtained,

$$S(t) = S_{mix} * h_{LP} \simeq \frac{1}{2}A_{src}(t)A_{det}(t) \cos[\varphi(t)]. \quad (8)$$

In a real application, the mixed signal depends on the detector input to output signal behavior, $S_{out}(S_{det})$.

When the frequency is swept, each frequency is associated to a different phase-shift. The most used technique for sweeping the frequency is the FMCW (Frequency Modulated Continuous Wave) broadband reflectometry [6]. The frequency changes continuously in a frequency range of $[F_{min}, F_{max}]$ and the instantaneous frequency is ideally given by a linear time dependence in the form $\omega(t) = 2\pi[F_{min} + k_s t]$, where $k_s = (F_{max} - F_{min})/\Delta t$ is the sweeping rate and Δt is the sweeping time. The stationary state of each frequency is assumed to be achieved quickly when compared with the sweeping time. If the time of flight is much smaller than the sweeping time, there is an approximately direct correspondence between the time of measurement and the time of the emission. Thus is possible to associate the amplitude, phase-shift and group delay with the respective frequency. This is an important point in simulation due to the compromise between this assumption and the reduction of the simulation time, especially in 3D.

Different techniques have been developed to extract the phase and the group delay from the detected signals [26, 27, 28, 25]. The most common method used to determine the time-delay within the homodyne-detection scheme is computing the time-varying frequency distribution of the output filtered signal using techniques such as the Sliding Fast Fourier Transform (SFFT technique). The time derivative of the phase represents the instant frequency of the $\cos[\varphi(t)]$ term, corresponding to the instantaneous beating frequency, $f_B(t)$. The group delay is calculated by

$$\tau_g = \frac{\partial \varphi}{\partial \omega} = \frac{1}{2\pi} \frac{\partial \varphi}{\partial t} \left(\frac{\partial f}{\partial t} \right)^{-1} = \frac{f_B}{2\pi k_s}. \quad (9)$$

The standard spectral techniques use the main frequency of each Fourier transform to estimate the beating frequency (maximum peak technique). The measurement of the absolute phase shift is possible with the in-phased and quadrature (IQ) detection scheme, represented in figure 1 (b). This scheme introduces a third signal corresponding to $S_{src}(t)$ or $S_{det}(t)$ shifted 90° . The three signals can be combined in different ways to obtain the phase and the amplitude. For example, with a 90° shifted source signal $S_{src}^{\pi/2}(t)$, the LPF (Low-Pass Filter) filtered I/Q signals are

$$I(t) = S_{det}(t)S_{src}^{\pi/2}(t) = \frac{1}{2}A_{src}A_{det}(t) \sin[\varphi(t)] \quad (10)$$

$$Q(t) = S_{det}(t)S_{src}(t) = \frac{1}{2}A_{src}A_{det}(t) \cos[\varphi(t)]. \quad (11)$$

From this system of equations the phase and the amplitude are directly given by

$$\varphi(t) = \arctan\left(\frac{Q(t)}{I(t)}\right) \quad (12)$$

$$A_{det}(t) = 2\sqrt{I^2(t) + Q^2(t)}. \quad (13)$$

The group delay is proportional to the time derivative of the phase and to the inverse of the sweeping rate:

$$\tau_g = \frac{1}{2\pi} \frac{\partial \varphi}{\partial f} = \frac{1}{2\pi} \left(\frac{\partial f}{\partial t} \right)^{-1} \frac{\partial \varphi}{\partial t} = \frac{1}{2\pi k_s} \frac{\partial \varphi}{\partial t}. \quad (14)$$

Throughout this work this method is referred as the IQ technique. From the experimental standpoint, the In-phased and Quadrature detection scheme has limitations. To increase the dynamic range of reflectometers and the signal-to-noise ratio, heterodyne detection techniques have been implemented [22].

The inversion technique is applied after the contribution from the propagation inside the microwave circuit is subtracted from the measured delay. The measured group delay is the sum of all the contributions of the propagation from the source to the detection point,

$$\tau_m(f) = \tau_{s \rightarrow a}(f) + 2\tau_{a \rightarrow p}(f) + 2\tau_{p \rightarrow c}(f) + \tau_{a \rightarrow d}(f), \quad (15)$$

where s labels the source, a the reference point (e.g. antenna mouth or wall), p the initial plasma position, c the cutoff position and d the detection position. The corrected group delay τ_c to be used by the inversion technique is

$$\tau(f) = \tau_m(f) - \tau_c(f), \quad (16)$$

where $\tau_c = \tau_{s \rightarrow a} + \tau_{a \rightarrow d}$. One experimental method to determine τ_c is place a metallic mirror at a known distance in the front of the reflectometer antennas. The time delay is measured for different mirror positions to minimize the error of free space propagation. In reflectometry simulation, an additional simulation is also necessary with the mirror to estimate this factor. The propagation time due to the distance between the antenna and the metallic mirror is removed from all measurements. The time-delays are then fit to the rectangular waveguide delay function,

$$\tau_c(f) = a + \frac{b}{\sqrt{1 - \left(\frac{f_c}{f}\right)^2}}, \quad (17)$$

where a and b are the fit parameters and f_c the cutoff frequency of the waveguide propagating mode. A constant a is added to include the propagation in vacuum depending on the reference position.

2.3. The position error and the amplitude of the detected signal

The Abel inversion algorithm assumes the validity conditions of the WKB phase expression and the monotonicity of the density profile [21]. However, in a real reflectometer, each one of these conditions may not be exactly valid due to different reasons, resulting in a measurement error. The position error $e(F)$ is defined as

$$e(F) = r_m(F) - r_0(F). \quad (18)$$

Here, $r_0(F)$ represents the real plasma position and r_m the measured position obtained after the application of the inversion technique using the corrected group delay. The position error $e(F)$ and the amplitude of the detected signal $A_{\text{det}}(F)$ are two fundamental quantities that characterize the measurement quality of a reflectometer for conventional/position reflectometry. An ideal reflectometer corresponds to $e(F) = 0$ and $A_{\text{det}}(F) = A_{\text{src}}(F)$. If the plasma is known, the error can be estimated with the help of numerical simulations and be used to demonstrate the system's viability and reliability. The error sources can be classified into two categories: (i) propagation and (ii) detection and data analysis. The propagation error sources occur from the signal excitation to detection and include the propagation in the experimental setup and in the plasma. The detection and data processing error sources occur in the detection process, during the signal acquisition, in the group delay estimation, in the implementation of the inversion algorithm and with the definition of the line of sight. The error sources are listed and described as follows:

- **Propagation in the plasma** - magnetically confining a plasma requires closed magnetic surfaces, implying, in general, some degree of curvature and divergence of the isodensity lines and gradients with variable direction along the propagation direction [29]. When propagating through irregular plasmas, various phenomena such as refraction, diffraction, scattering, wave trapping or resonance absorption can affect the probing wave [30, 31]. These effects lead to changes in the propagation path, resulting in variations in the group delay and in the amplitude of the detected signal. Apart from the equilibrium plasma shape, other phenomena such as turbulence or MHD instabilities (e.g. vertical plasma displacements or ELMs) introduce significant local or macroscopical variations in the density profiles during the discharges, affecting the propagation of the probing beam. During the ramp-up/down phases the electron density profile is being formed, which can further complicate the plasma

probing under the validity conditions. In case of higher temperatures, the relativistic corrections should be implemented to avoid intrinsic errors arising from an inappropriate interpretative model [14]. If the Doppler effect becomes relevant, the propagation is also affected [32].

- **Probing beam** - in a real reflectometer, the probing beam is influenced by the radiation pattern of the antenna, which is frequency dependent in general. The spatial and temporal configuration of the beam impact the interaction with the plasma, leading to different reflected signals from the same probed plasma. If the antenna is placed at a cavity surrounded by a metallic structure, undesired lobes can be generated, which later are reflected and detected by the receiving antenna [33]. The propagation of the probing beam can also be affected if its electromagnetic field is not aligned with the magnetic field as required by the probing mode. The magnetic fluctuations are typically small, and its effect on the signal is neglectable. Additionally, the assumption of a linear probing frequency is often used, but in practice, there are nonlinearities that affect the measurement. Recently, a technique to monitor and re-calibrate in real-time the linearity of the frequency sweeps of FMCW reflectometers was developed [34].
- **Plasma-wall reflections** - the reflected wave is a superposition of electric field coming from different locations, which are fully taken into account in 3D full-wave simulations if a realistic plasma/setup models are given as input. When the power is reflected from the plasma, a portion of it enters at the receiving antenna(s) for detection, another portion is reflected at the surrounding wall back to the plasma, and some energy is lost in other directions. The energy that is reflected back into the plasma undergoes another process of propagation. This process can occur multiple times resulting in delayed detection of the reflected signals. The reflected signals enter the antenna and propagate through the oversized waveguide where resonances and reflections can occur until they are converted to a fundamental mode to be detected. These effects influence the amplitude of the detected signal and can interfere with the estimation of the group delay.
- **Inversion algorithm** - the numerical discretization introduces inherent error to the position measurements. The density resolution of the reflectometer depends on the frequency resolution of the acquisition, given by $\Delta F = k_s/f_s$, where f_s is the sampling frequency. In O-mode the resolution is directly calculated as $\Delta n = 2f\Delta F/\alpha_0$. In X-mode, the resolution also depends on the magnetic field. The inversion algorithm, especially in O-mode and upper cutoff X-mode, requires an initialization method. Theoretically the frequency should be swept in the $0 - F$ range but in practice the phase derivative is initialised from 0 up to the initialization frequency F_i , known as the first frequency. The first frequency is typically the initial frequency of the first band used to probe the plasma. The group delay used to obtain the density profile is described by a piecewise function so the plasma position is written in the form

$$x_c(F) = x_p + \frac{c}{\pi} \int_0^{F_i} \frac{\tau_i(f)}{\sqrt{F^2 - f^2}} df + \frac{c}{\pi} \int_{F_i}^F \frac{\tau_m(f)}{\sqrt{F^2 - f^2}} df = I(\tau_i, F_i, F) + \frac{c}{\pi} \int_{F_i}^F \frac{\tau_m(f)}{\sqrt{F^2 - f^2}} df,$$

resulting in an intrinsic error to the measurement. The position error depends on the initialization function, τ_i , introduced in $I(\tau_i, F_i, F)$. It is reduced for higher frequencies and lower initialization frequencies. There are three forms of initializing the group delay profile. The first possibility is to use data from other diagnostics. The second option is the use of data from the X-mode density profile reconstruction. The last option, ideal for PPR systems, is the use of a physical model for the group delay, as it is proposed in [35].

- **Line of sight** - The reference plasma position depends on the density profile along the line of sight, which can result in a variation in the position error for the same group delay. The line of sight is typically chosen in the direction of the probing beam. In this case, if the plasma is close to the ideal model, the error is minimized.

The data analysis techniques aim to reduce the absolute value of the measurement error by correcting the group delay. The group delay can be decomposed into a smooth term (τ_0) and fluctuations ($\tilde{\tau}$), given by the equation

$$\tau(F) = \tau_0(F) + \tilde{\tau}(F). \quad (19)$$

Various techniques have been developed to remove the fluctuations $\tilde{\tau}$ and improve the smoothness of the group delay. One commonly used method is the best path method or the first moment of the beating frequency, which is applied instead of the frequency with maximum amplitude [25]. However, the correction process becomes more complex

when the smooth term itself contains intrinsic errors. Artificial neural networks have been used in reflectometry signal analysis to obtain smooth density profile reconstructions [36]. In a recent study [37], a reconstruction scheme utilizing a database with the perturbation shapes was applied to density profiles with non-monotonic regions, resulting in an improved description of the density profiles. Reflectometry reconstruction techniques continue to be an important area of research in the field.

2.4. Notation to describe multi reflectometers systems

Due to the complexity arising from the high number of variables and signals in the analysis of a PPR system, or, in general, a multi-reflectometers system (MRS), we propose a notation with dependent indeces. With this notation it is possible to organize the variables and structure the computational framework of functions to automate the simulation and data analysis of PPR systems. Each signal or variable a used in the description of a reflectometer is written in the form

$$a_{\text{label}}^{\text{MRS indeces}}(\text{input variables of } a) = f[\text{input variables of } f], \quad (20)$$

where the MRS indeces identify the reflectometer and other important variables, groups of variables, or subsystems of the MRS system. The label simplifies the variable description, and f represents the dependence (e.g. function or operator). The input independent variables of a are enclosed by parentheses and the input variables of f by square brackets. Each index is numbered as $i = 1, \dots, N_i$, where N_i is the number of elements associated to the index i , dependent on the previous indeces. Thus the order of index is generally important. For example, if three indeces are defined, i, j and k , N_i is independent since it is associated with the first one, but $N_j(i)$ and $N_k(i, j)$ become functions of the previous indeces in general. If is necessary to describe a vector with all the elements associated with index i , the index is represented on the left side and the variable symbol becomes bold (usual notation for vector):

$$a^i \rightarrow {}^i \mathbf{a} = (a^1, \dots, a^{N_i}) \quad (21)$$

With this notation, it is implicit that i is the index that distinguish the vector elements. If \mathbf{a} is used with the suppressed index, it is necessary to know beforehand that the elements were differentiated by i . If the variable depends on multiple indices and only a part of them is used in the vector, the elements are organized based on the order of the indices. Let's consider a variable labeled with three indices, i, j and k , and the vector is created with the indices i and j . In this case, we write:

$$a^{ijk} \rightarrow {}^{jk} \mathbf{a}^i = \mathbf{a}^i = (a^{i1}, \dots, a^{iN_j(i)1}, \dots, a^{iN_k(i,j)}, \dots, a^{iN_j(i)N_k(i,j)}). \quad (22)$$

If N_j and N_k are dependent, the vector length changes according to i . The total number of elements of a variable a in the system is

$$N[a^{ijk\dots n}] = \sum_{i=1}^{N_i} \sum_{j=1}^{N_j(i)} \sum_{k=1}^{N_k(i,j)} \dots N_n(i, j, k, \dots). \quad (23)$$

Using this notation, we proceed to the study of a system of multiple reflectometers. The same letter f is used multiple multiple times to represent the dependence of different variables.

2.5. Description of systems of multiple reflectometers

A multiple reflectometers system or multi-reflectometers system (MRS) is defined as a system of N_R reflectometers operating in the presence of a plasma. Each reflectometer in the MRS is labeled with the index $i = 1, \dots, N_R$ and comprises $N_S(i)$ sources, labeled by the index j , $N_D(i)$ detectors and $N_A(i)$ antennas. The total number of detectors associated to a specific source is $N_d(i, j)$, labeled with l . A microwave circuit connects all these elements, and their interdependence is determined by the reflectometer's specific architecture. In general, a detector refers to all the physical hardware that transforms a reference signal and the received signal from the plasma into an output electric signal suitable for digital conversion and analysis. This description applies to different reflectometer architectures. Typically, each detector detects the signal associated with a source, and multiple detectors can detect signals from the same source. During the operation, a reflectometer provides the measurement at each instant $t_m = kT_m$, where $k = 1, \dots, N_m$. Here, T_m is the measurement duration and N_m the total number of measurements during the operation. The operation duration $T_O = N_m T_m$ is not necessarily the same as the plasma discharge time, as diagnostic systems often start before plasma formation and continue after the plasma discharge ends. Each measurement consists in

two phases: the probing phase and the processing phase. At instant t_m , the output of the previous measurement is available in the corresponding hardware location. The new measurement begins, and all the necessary mechanisms for microwave emission are activated, emitting the probing signal from the sources. Simultaneously, the reflected signal is detected and digitally recorded. These processes comprise the probing phase, which occurs during the time interval T_{prob} and concludes at instant $t_m + T_{prob}$. In the second phase, during the time interval T_{proc} , the signals are processed, and position measurements are calculated using inversion algorithms. The total measurement duration is determined by the sum of the time durations of the two phases and can be expressed as:

$$T_m = T_{measuring} = T_{probing} + T_{processing}. \quad (24)$$

The rate of measurement is $f_m = 1/T_m$. The time variable associated with the k -th measurement is given by:

$$t = t_m + \underline{t}T_m = (k + \underline{t})T_m, \quad (25)$$

with $\underline{t} \in [0, 1]$. In an ideal PPR, it is assumed that all the reflectometers are synchronized and are characterized by the same T_m , T_{prob} and T_{proc} . However, achieving perfect synchronization in experiments is not always straightforward. The main indices used to describe a MRS variable are i, j, l, k , corresponding to the reflectometer, source, detector and the measurement index. Figure 2 provides a schematic representation of the different signals and variables involved in a reflectometer of an MRS.

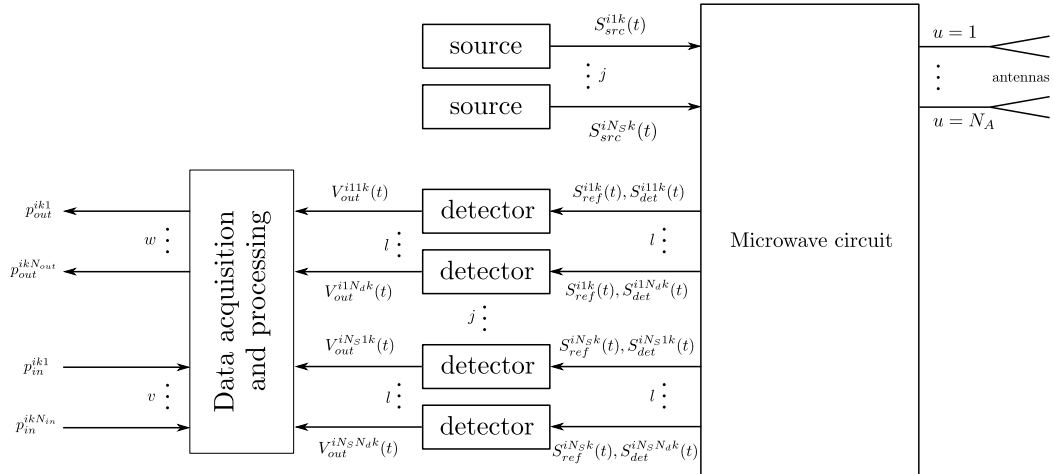


Fig. 2: Schematic view of the different signals and variables of a reflectometer used in the description of a MRS.

The microwave sources excite the fundamental mode $\mathbf{E}_S^{ijk}(\mathbf{r}, t)$ of a fundamental waveguide, characterized by a specific temporal dependence, $S_{src}^{ijk}(t)$, known as the source signal. The fundamental mode can be written as:

$$\mathbf{E}_S^{ijk}(\mathbf{r}, t) = \mathbf{E}_S^{ijk}(\mathbf{r})S_{src}^{ijk}(t), \quad (26)$$

where $\mathbf{E}_S^{ijk}(\mathbf{r})$ is normalized to its maximum value in the waveguide cross-section. The source signal $S_{src}^{ijk}(t)$ contains information about the maximum field amplitude. In FMCW reflectometry, this function takes the form of equation (5), and $A_{src}(t)$ represents the amplitude of the electric field. Typically, there is one source per band, and the number of bands N_B is equal to the number of sources, $N_B = N_S$, with the bands also labeled by the index j . The source signal can be expressed as a function of the minimum and maximum frequencies of the respective band, as well as the sweeping time T_{sw} :

$$S_{src}^{ijk}(t) = S_{src}^{ijk}[f_{min}^{ij}, f_{max}^{ij}, T_{sw}^{ij}, t]. \quad (27)$$

The detector returns the output electric signal $S_{out}^{ijk}(t)$ from the reference electromagnetic signal $\mathbf{E}_R^{ijk}(\mathbf{r}, t)$ and from the signal received from the plasma, $\mathbf{E}_D^{ijk}(\mathbf{r}, t)$. These electromagnetic signals correspond to fundamental waveguide

modes and can be written in the form of equation (26):

$$\mathbf{E}_R^{ijk}(\mathbf{r}, t) = \mathbf{E}_R^{ijk}(\mathbf{r}) S_{ref}^{ijk}(t) \quad (28)$$

$$\mathbf{E}_D^{ijk}(\mathbf{r}, t) = \mathbf{E}_D^{ijk}(\mathbf{r}) S_{det}^{ijk}(t), \quad (29)$$

where $S_{ref}^{ijk}(t)$ and $S_{det}^{ijk}(t)$ are the reference and detected signals which include information on the amplitude of the electric field. The output electric signal is

$$S_{out}^{ijk}(t) = D \left[S_{ref}^{ijk}(t), S_{det}^{ijk}(t) \right] \quad (30)$$

where D is the detector operator that depends on the detector architecture. Typically, the reference signal is given in terms of the source signal, $S_{ref}^{ijk}(t) = S_{src}^{ijk}(t)$.

The dynamic of a MRS system is described by the macroscopic Maxwell's equations and a plasma fluid model. In fusion applications, the cold plasma equation of motion without the collisional term is commonly used to describe the plasma. The input plasma parameters are the density and the magnetic field. The plasma temperature can be included to take into account the relativistic effects, dominant for the O-mode [14]. The MRS metallic structure where the fields propagate is described by a conductivity function, $\sigma(\mathbf{r})$. The solution of the system of differential equations that describe the propagation of the electromagnetic field depends on several factors, including the $S_{src}^{ijk}(t)$ signal, on the conductivity $\sigma(\mathbf{r})$, on the electron density $n_e(\mathbf{r}, t)$ and on the confinement magnetic field $\mathbf{B}_0(\mathbf{r}, t)$. The detected signal is written as a function of these physical variables:

$$S_{det}^{ijk}(t) = f[S_{src}^{ijk}(t), \sigma(\mathbf{r}), n_e(\mathbf{r}, t), \mathbf{B}_0(\mathbf{r}, t)] \quad (31)$$

The total number of detected signals in the system during a measurement sequence is given by:

$$N_{det} = \sum_i^{N_R} \left[\sum_j^{N_S(i)} N_d(i, j) N_m(i) \right]. \quad (32)$$

The simulation of a PPR configuration involves obtaining numerically all these signals. The arguments of f in equation (31) represent the input parameters of the simulation, while the left side represents the output signal.

2.6. Acquisition and data processing in PPR systems

The acquisition and data processing are described by the operator F . In this process, the output signals from different detectors are converted to discrete-time signals, and the data is processed using various techniques to estimate the plasma position or other parameters. In some cases, additional input data is required, for example, the data of other diagnostic, geometry parameters, or the initialization function. Considering $N_{in}(i)$ inputs p_{in}^{ikv} , labeled with v , and $N_{out}(i)$ output parameters, labeled by w , the output plasma parameter p_{out}^{ikw} is given by

$$p_{out}^{ikw} = F^{iw} \left[S_{out}^{ik}, p_{in}^{ik} \right], \quad (33)$$

where $S_{out}^{ik} = {}^j S_{out}^{ik}$, $p_{in}^{ik} = {}^v p_{in}^{ik}$, and the operation F depends on the reflectometer and the parameter to be calculated. This is a general expression, valid for different reflectometry techniques. For PPR systems, the measurement of the plasma position involves four phases:

1. **Group delay extraction** - The group delay of each band is obtained by applying a phase derivative extraction technique (P) to the output signals,

$$\tau_c^{ijk}(F) = P^i \left[S_{out}^{ijk}(t), \tau_c^j(F), p_P^{ik} \right]. \quad (34)$$

Here $\tau_c^{ij} = {}^l \tau_c^{ij}$ is the group delay correction relative to the propagation in the reflectometer microwave circuit. p_P^{ik} corresponds to the input parameters associated with the extraction operation, such as signal filter parameters. In the case of multiple receiving antennas in different positions, the group delay correction can be applied

separately. A line of sight is associated with each detection, described by the parametrization

$$\mathbf{r}_{ls}^{ijl} = \mathbf{r}_{ls0}^{ijl} + \alpha^{ijl} \mathbf{v}_{ls}^{ijl}, \quad (35)$$

where α is the parametrization variable, \mathbf{r}_{ls0} the reference and \mathbf{v}_{ls} a normalized vector with the line direction.

2. **Group delay assembly** - The group delays of the different bands are concatenated and an initialization technique is applied, if required. This operation is described by J :

$$\tau_{FB}^{ik}(F) = J^i \left[\tau^{ik}(F), \mathbf{p}_J^{ik} \right], \quad (36)$$

where $\tau_{FB}(F)$ is the Full-Band (FB) group delay. \mathbf{p}_J^{ik} contains complementary input parameters associated with J , for example for the overlap over the probing frequency bandwidth or the initialization function. If multiple antennas are involved an algorithm is applied to obtain a single $\tau_{FB}(F)$ profile.

3. **Inversion technique** - The relative position is obtained from the group delay by the inversion technique I ,

$$r_m^{ik}(F) = I^i \left[\tau_{FB}^{ik}(F), \mathbf{p}_I^{ik} \right], \quad (37)$$

where \mathbf{p}_I^{ik} are additional input parameters associated with I (e.g. initial plasma position or group delay).

4. **Plasma position** - The inversion method determines the relative cutoff position. The definition of the final plasma position requires the specification of an arbitrary reference line of sight. If the reference line is defined along the direction of the main lobe of the probing beam, the measured position corresponds to the actual position of the plasma along the line of sight, assuming ideal propagation. The final position of the cutoff layer is given by

$$\mathbf{r}^{ik}(F_{sep}) = \mathbf{r}_{ref}^i + r_m^{ik}(F_{sep}) \mathbf{v}_{ref}^i, \quad (38)$$

where F_{sep} is the separatrix frequency, $F_{sep} = \sqrt{\alpha_0 n_{sep}}$, \mathbf{r}_{ref}^i the reference position (see equation (15)) in the reference line of view and \mathbf{v}_{ref}^i a unitary vector indicating the direction of the reference line of sight. In the case of multiple measurement subsystems within the same reflectometer, the position error is individually defined for each subsystem.

Defining the real position of the plasma in the reference line of sight as $r_0^{ik}(F_{sep})$, the difference of the measured position and the real position r_m^{ik} is

$$\mathbf{r}^{ik}(F_{sep}) - \mathbf{r}_0^{ik}(F_{sep}) = [r_m^{ik}(F_{sep}) - r_0^{ik}(F_{sep})] \mathbf{v}_{ref}^i, \quad (39)$$

the position error is defined as

$$e^{ik}(F) = [\mathbf{r}^{ik}(F) - \mathbf{r}_0^{ik}(F)] \cdot \mathbf{v}_{ref}^i = r_m^{ik}(F) - r_0^{ik}(F). \quad (40)$$

Considering the four steps of the data analysis, the dependence of the position error is

$$e^{ik}(F) = E^i [\mathbf{S}_{src}^{ik}(t), \boldsymbol{\tau}_c^i(F), \sigma(\mathbf{r}), n_e(\mathbf{r}, t), \mathbf{B}_0(\mathbf{r}, t), \mathbf{r}_{ref}^i, \mathbf{v}_{ref}^i, \mathbf{p}_m^{ik}], \quad (41)$$

and of the relative detected signal amplitude, normalized to the source amplitude, is

$$a^{ik}(F) = A[\mathbf{S}_{src}^{ik}(t), \sigma(\mathbf{r}), n_e(\mathbf{r}, t), \mathbf{B}_0(\mathbf{r}, t)]. \quad (42)$$

To study a PPR (Plasma Position Reflectometry) configuration, it is necessary to calculate the position error and the detected amplitude from the simulated signals for all reflectometers. The difficulty of this process lies in the definition of the input parameters used in the reconstruction techniques.

2.7. Multiple configurations of reflectometers

The design and optimization of a PPR system requires the comparison of multiple configurations of N_R reflectometers, with different geometries and orientations, in different plasmas. For this purpose, we introduce two new indices, the

plasma index denoted by $p = 1, \dots, N_p$, and the reflectometer system configuration index, denoted by $c = 1, \dots, N_c$. Both indices are independent of each other. The expression 31 can be written as follows:

$$S_{det}^{ijlcpk}(t) = f[S_{src}^{ijk}(t), \sigma^c(\mathbf{r}), n_e^p(\mathbf{r}, t), \mathbf{B}_0^p(\mathbf{r}, t)]. \quad (43)$$

Similarly, the position error and the detected amplitude in the form can be expressed as:

$$\begin{aligned} e^{icpk}(F) &= E^i[S_{src}^{ik}(t), \tau_c^i(F), \sigma^c(\mathbf{r}), n_e^p(\mathbf{r}, t), \mathbf{B}_0^p(\mathbf{r}, t), \mathbf{r}_{ref}^i, \mathbf{v}_{ref}^i, \mathbf{p}_{in}^{ik}], \\ a^{icpk}(F) &= A[S_{src}^{ik}(t), \sigma^c(\mathbf{r}), n_e^p(\mathbf{r}, t), \mathbf{B}_0^p(\mathbf{r}, t)]. \end{aligned} \quad (44)$$

To study multiple configurations of a PPR system it is necessary to simulate the $S_{det}^{ijlcpk}(t)$ signals and calculate the detected amplitude $a^{icpk}(F)$ and the position error $e^{icpk}(F)$ for each configuration. Automating the simulation process and data processing is essential for conducting the optimization or the parametric scan studies effectively. In the following section, we propose a framework to automate the simulation process, while the automation of data analysis is discussed in section four.

3. Simulation of multi reflectometers systems

3.1. The REFMUL* family of FDTD codes for reflectometry simulation

3.1.1. Reflectometry simulation with FDTD codes

The Finite-Differences Time-Domain (FDTD) method, or Yee's method, has been one of the most widely adopted solutions to study reflectometry systems [38, 16, 39]. The simulation of reflectometry measurements is possible by coupling the Maxwell's equations with the linear cold plasma model [40],

$$\frac{\partial \mathbf{J}}{\partial t} = \varepsilon_0 \omega_p^2(\mathbf{r}) \mathbf{E} + \omega_c(\mathbf{r}) [\mathbf{b} \times \mathbf{J}], \quad (46)$$

where \mathbf{b} is a unit vector with the direction of the magnetic field, ω_p is the plasma frequency and ω_c the electron cyclotron frequency. A model for the discretization of equation (46) is derived in [41]. In [42] it has been shown that the X-mode (TE_z) standard algorithm can become unstable with strong gradients in the plasma parameters after. This instability worsens as the turbulence level increases. The authors have proposed new coupling schemes to extend the stable time steps for values in the order of millions of iterations.

Typically, the codes that utilize Cartesian coordinates apply the algorithm in a region defined by a parallelepiped-rectangle characterized by the length of each side, l_x , l_y and l_z . This region, known as the region of the interest (ROI), contains the physically relevant elements for the final result. A common practice that simplifies the FDTD algorithm implementation is to use of the same spatial step in all directions, $\Delta = \Delta x = \Delta y = \Delta z$. The resolution is represented by the number of points per wavelength for each dimension, $N_\lambda = \lambda/\Delta$ and by the number of points per period, $N_T = T/\Delta t$, where Δt is the time step. As the number of points per wavelength and period increases, the phase velocity approaches the speed of light and becomes independent of the direction [43]. These parameters are adjusted according to the Courant-Friedrichs-Lewy condition for numerical stability,

$$S = N_\lambda/N_T < S_{\max}. \quad (47)$$

In three dimensions, $S_{\max} = 1/\sqrt{3}$, in two dimensions, $S_{\max} = 1/\sqrt{2}$, and in one dimension, $S_{\max} = 1$ (known as the magic step to avoid numerical dispersion). Given a grid reference frequency, $f_0 = 1/T$, the number of points of each grid dimension is:

$$N_{x,y,z} = \text{floor} \left[\frac{l_{x,y,z}}{\Delta} \right] = \text{floor} \left[l_{x,y,z} N_\lambda \frac{f_0}{c} \right]. \quad (48)$$

where floor returns the nearest integer value. The number of iterations N_{it} determines the simulated physical time,

$$T_s = N_{it} \Delta t = \frac{N_{it}}{N_T f_0}. \quad (49)$$

3.1.2. The REFMUL* family of codes and the simulation setup

REFMUL* is a family of time-dependent codes primarily designed for microwave reflectometry research. These codes consider various factors, including the wave propagation in time-dependent plasmas, the structure of the vacuum vessel, and the waveguides and antennas of the reflectometer. The REFMUL* family of codes includes the (i) REFMUL, a 2D O-mode (TM_z) code [44], (ii) REFMULX/REFMULXp, a 2D X-mode (TE_z) simulation code [45], (iii) REFMULF, a 2D OpenMP [46] full polarization code and (iv) REFMUL3, a 3D hybrid OpenMP/MPI [47] full-wave code [15]. REFMUL* codes have been extensively used in studies involving ASDEX Upgrade, Tore Supra [15], ITER for the design of the PPR system [16], and for assessing microwave diagnostics for DEMO [17]. Figure 3 shows the scheme of a 2D REFMUL simulation setup with the snapshot of the positive part of the electric field at $f = 28$ GHz where it is possible to observe the multiple plasma-wall reflections resulting from the interaction of the probing beam with the plasma. This simulation uses a region of interest of dimensions $l_x = 1.2 \text{ m} \times l_y = 1 \text{ m}$, corresponding to 3363×2803 grid points for a reference frequency of $f_0 = 29$ GHz. The slab electron density model corresponds to an exponential decay of 1.5 cm from the LFS region separatrix point of the 2017 DEMO density model provided by the EUROfusion database [48].

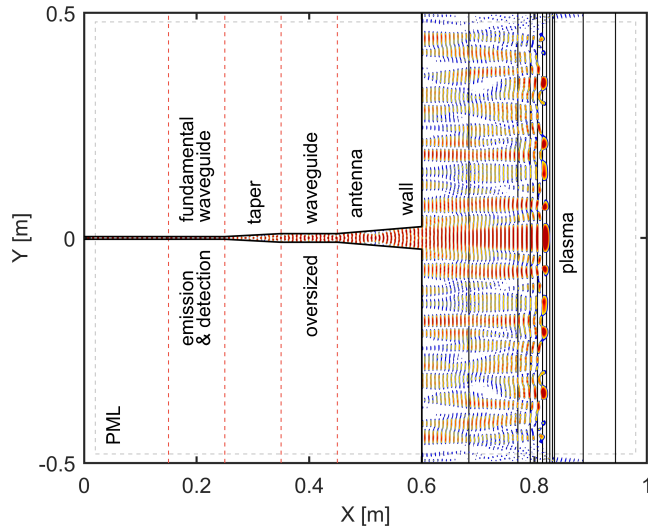


Fig. 3: Scheme of a 2D REFMUL simulation setup with the snapshot of the positive part of the electric field.

The simulation setup is common across different versions and dimensions, comprising four main elements: (i) the metallic structure, (ii) the plasma, (iii) the vacuum region, and (iv) the Perfectly Matched Layer (PML) [39]. The input is defined in Cartesian coordinates following the Finite-Difference Time-Domain (FDTD) formulation.

The metallic structure includes the antenna setup (the waveguides, the tapers, the antennas) and the surrounding structure, and is considered a perfect conductor. A perfect conductor is easily computationally implemented if the structure is described by a binary tensor. The electric field values are multiplied by the elements of this tensor, resulting in zero values within the perfect conductor region, thus simplifying the algorithm. The conductivity tensor is denoted as $\sigma_S(i, j, k)$, where i, j , and k represent the grid point indices, and it has the same dimensions as the FDTD grid. The plasma is characterized by a density tensor, $n_e(i, j, k)$, and the magnetic field, $\mathbf{B}_0(i, j, k)$.

Since the FDTD algorithm relies on knowledge of the fields at adjacent cells, simulated waves would be reflected at the boundary due to the electric field at the boundary cells always being zero [43]. To address this issue, a Perfectly Matched Layer (PML) is placed around the FDTD grid, which absorbs incident waves originating from a vacuum region [49]. A transition frame is applied to the plasma properties to ensure a vacuum region exists before the PML [39]. The wave is excited in a fundamental waveguide, allowing for the detection and emission of the fundamental mode. When the electromagnetic field is locally excited within the grid to generate a probing signal, the excited field propagates in all possible directions [43]. The excitation of the fundamental mode in the waveguide with a soft source generates two waves propagating in opposite directions, making it challenging to measure the reflected signal in mono-static systems. The solution to this problem is the use of a unidirectional transparent source (UTS) [44]. This algorithm enables signal emission in one direction and signal detection in the other, making it ideal for

reflectometry simulations. The signal is injected into the fundamental waveguide, where it is also detected in the case of a mono-static system. The waveguide cross-section is assumed to be rectangular, and the source dimensions are determined by the number of points on each side of the rectangle. The field is excited in a y - z plane defined by i_{src} (x -axis) and a minimum and maximum value of j (y -axis) and k (z -axis) indices, respectively, denoted as $[j_{min}, j_{max}]$ and $[k_{min}, k_{max}]$. Details of the signal injection and detection can be found in appendix A and B. With the UTS implemented, the detection at a mono-static reflectometer can be performed at the coordinates:

$$r_{det} = (i_{det}, j_{det}, k_{det}) = (i_{src}, j_{src}, k_{src}) - (1, 0, 0). \quad (50)$$

Both homodyne and IQ detection signals can be simulated with a single simulation.

3.2. Formulation of a high-level framework for multi-reflectometry simulations

3.2.1. The need of a high-level framework for reflectometry simulation

The simulation of a reflectometry measurement for a plasma/reflectometer configuration and a specific band involves five elementary sequential operations:

1. **Input models** - Create input models for the plasma and metallic structure within the region of interest based on input data. Define the source characteristics, detection points, and line of view. Adapt the fundamental waveguide to the simulated band (see appendix A and B).
2. **UTS impulse response** - Compute the unidirectional transparent source (UTS) impulse response in vacuum for the given metallic structure.
3. **Mirror calibration** - Run the setup in vacuum and place a mirror at a reference position to determine the group delay associated with the propagation inside the antenna setup.
4. **Simulation with the plasma** - Run the simulation with the plasma and record the detected signal, S_{det} .
5. **Source signals** - Obtain the source signal to be used as reference in the data analysis, S_{src} . In case of a IQ detection, the 90° shifted signal is also required.

Suppose the reflectometer operates in N_B bands (each with a different f_0). It is necessary to generate N_B models for the metallic structure and N_B plasma models, compute N_B UTS impulse responses, perform N_B simulations with the mirror, and run N_B simulations with the plasma. Each band is associated with a different FDTD grid. The data processing for PPR systems requires finding N_B group delays (in the case of a mono-static configuration) and combining them into a single full-band dataset to apply the inversion algorithm.

As discussed in section 2, the study and optimization of PPR systems involves testing different plasma and geometry configurations of different MRSs. These simulation and data processing steps need to be repeated for different reflectometers, regions of interest, plasmas, metallic structures, and bands. This task is computationally demanding and time-consuming in terms of model generation and script development. Therefore, the optimization of PPR systems requires a high-level framework that simplifies and automates these operations, including the management of simulations on high-performance computers (HPCs).

3.2.2. Formulation of a high-level framework for reflectometry simulations

The framework should be designed to:

1. automate the generation of discrete models required for simulations based on the input plasma, reflectometer/MRS models;
2. automate the simulation process, including the creation of scripts for UTS impulse response simulations, mirror simulations, plasma simulations, and reference signal generation;
3. simplify the input definition process, allowing easy specification of regions of interest, reflectometer models, and plasma configurations to enable simulations of multiple configurations within the available time;
4. support different versions of REFMUL with varying dimensions (1D, 2D, 3D);
5. automate the data processing, enabling the optimization of PPRs, statistical studies of various plasma configurations, and other related analyses;

6. provide the necessary scripts to facilitate these tasks, such as running simulations, managing them on HPCs, data verification, and control of other operations.

Apart from these functionalities, the framework should facilitate the integration of different users. Different elements of the research team can contribute to the same project. The structure of the framework should be designed to easily implement different functions for designing the input models and different system parameters. We propose a framework structure that is compatible with all these requirements. Simulating a set of independent simulations and processing and analyzing the results is simply a matter of defining the input configurations and running a few scripts. The procedure for running and processing a set of independent simulations is represented in figure 4.

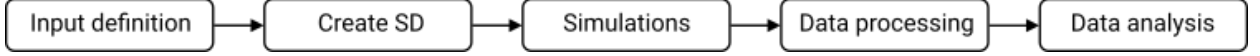


Fig. 4: The five phases of the procedure.

The workflow consists of five phases. In the first phase, the user defines the input data, including regions of interest, plasmas, reflectometer geometries, probing bands, and other relevant variables for the simulations. In the second phase, a code runs to create the simulation directory (SD), which contains all the necessary data (models, scripts, data lists) for running the simulations and analyzing the results based on the input. The third phase involves running the simulations using the respective scripts. This begins with running the simulations to find the UTS impulsive response, and then the independent simulations with the plasma/mirror are distributed across different processing units. Once the simulations are completed, the data processing scripts read the input data and process the simulation data, saving the final results in the output directory (fourth phase). Finally, in the last phase, the user can plot the results and analyse the data based on the specific problem they are studying. This step can also be automated for different types of studies if the input follows a consistent format.

An important condition to simplify the framework and the output scripts is to assume that the source excitation occurs in a plane, as opposed to using an oblique UTS source. This simplifies the definition of the source position and the calculation of many variables, allowing for the simplification and optimization of various parts of the code. It also enables the definition of a pure mode, and the UTS algorithm is faster in this case compared to the oblique case. Therefore, it is necessary to implement the required frame conversion operations on the input data, so that they are defined in the simulation frame (discussed in section 3.4).

A basic concept for simulating automation would involve having a list of simulations as input, where each variable is defined in a different column. The code would then generate the necessary scripts to run the simulations one by one, corresponding to the signals given by equation (43). However, this approach does not optimize the time required to define the input as much as possible, as there are many variables to define for each simulation and there are simulations that share the same parameters. If we are simulating a set of N_R reflectometers probing N_P plasmas with N_B bands, it would require the definition of $N_R \times N_B \times N_P$ independent input lines, which would be a time-consuming task.

The solution is to identify key groups of independent input variables from which the other variables and operations of the problem are dependent. Each group is associated with a main variable that has an assigned value/identification, corresponding to a unique combination of input values. For example, if we are simulating a system of three reflectometers, where two of them use the K and Ka bands, and the third one uses the Ka and Q bands, then there are 6 different sources, corresponding to the pairs of indices (1,1), (1,2), (2,1), (2,2), (3,1), (3,2). Only three different groups of sources are distinct and need to be defined as input if we know the association for each pair. The main variable source would assume only three values/identifiers (K, Ka, Q). The pairs can be written in the form (1,K), (1,Ka), (2,K), (2,Ka), (3,Ka), (3,Q). All the variables and operations of the problem can be expressed as functions of main variables. It is possible to establish a mapping between the index values that label each variable of each simulation and a combination of values of the main variables. With this mapping, the input definition can be simplified by providing a list of input variable values associated with each value of the main variables. The list of simulations and other necessary lists can be generated automatically by considering combinations of values for the main variables. Many operations can be implemented using a for loop that iterates over the possible combinations in the list. Based in this principle, the next section discusses the necessary main variables to the simulation of a set of MRSs with FDTD codes of different dimensions.

3.2.3. Identification of the main variables of the problem

In Equation (43), the dependence of the detected signal of a given reflectometer of an MRS considered multiple configurations of geometry and plasma. The index i labels the reflectometer, j represents the source, l corresponds to the detector associated with source j , c denotes the reflectometer system configuration, p represents the plasma, and k indicates the measurement. However, in the context of simulations, these indices have limited usefulness due to several reasons. Firstly, (i) there are other important variables associated to the simulations (e.g. ROI variables). Then, (ii) every simulation corresponds to a measurement. The measurement index is associated with the simulated plasma model. Another aspect to consider is that (iii) only one source (band) is simulated each time. All the associated detectors can be simulated at the same time. Each simulation produces $N_d(i, j)$ detected signals. (iv) The plasma and reflectometer system configuration indices have variable length so we can simulate different MRSs and different plasmas for different reflectometers from the same input files. Finally, (v) depending on the application, the dimension of the simulation can be different (1D, 2D, 3D). Therefore the signals of each simulation must be identified with different indices.

Depending on the dimension, the REFMUL* version used to run the simulations is different, and the generation of models from the input data is carried out with different parameters or routines. In the context of simulations, the simulation dimension is represented by the D' index (ranging from 1 to 3), and the main variable D (1D, 2D, 3D). In general, for simulating a Multiple-Reflectometer System (MRS), a distinct Region of Interest is defined for each reflectometer/plasma combination. However, different plasmas can share the same ROI, simplifying the input definition. The ROI is labeled by the index R' and with the main variable R . Instead of using the j index, the source/band is labeled with the B' index, corresponding to the main variable B . The reflectometer index can be associated with the ROI, reducing the number of main variables required. The detector index is not used since different detections associated with a particular band can be simulated simultaneously.

The geometry of the metallic structure is labeled with the index S' and the main variable S . Note that when the geometry is mentioned, it is not associated with any specific input tensor for simulation, but with the geometry of the entire system, defined by the conductivity function, including all the reflectometers. The final model of the metallic structure to be used in the simulations depends on the region of interest, the reflectometer geometry, and the band being simulated. Similarly, the final plasma models depend on the region of interest and the simulated band. The group of plasma variables is labeled with the index P , which is equivalent to p used in the description of MRSs. Due to the fact the P' and S' indices are now dependent, the expression 43 becomes

$$S_{det}^{D'R'S'P'B'}(n) = f[S_{src}^{D'R'S'P'B'}(n), \sigma_S^{D'R'S'P'B'}(i, j, k, n), n_e^{D'R'S'P'B'}(i, j, k, n), \mathbf{B}_0^{D'R'S'P'B'}(i, j, k, n)] \quad (51)$$

for the simulated detected signal, in the case of the simulation of mono-static reflectometers, where n is the iteration number. The index order is arbitrary but has to be consistent, keeping in mind they are in general dependent from the previous ones. The dependence has the same form when multiple signals are detected. The left side represents the simulated signals and the right side the simulation and its main input parameters. All the variables used in the simulations depend on the particular combination of the $D'-R'-S'-P'-B'$ indices. Each $D'-R'-S'-P'-B'$ has a $D-R-S-P-B$ combination associated. The list of simulations is also given by all the possible $D-R-S-P-B$ combinations, which in number are the same. Many variables are only dependent on a subset of the main variables, simplifying the code. For example, the density model is not dependent on the input data available in S ,

$$n_e^{D'R'S'P'B'}(i, j, k, n) = f[D, R, P, B]. \quad (52)$$

All the different plasma models used in the simulations are associated with a $D-R-P-B$ combination. Equation (51) can be written in terms of the main variables values in the form

$$S_{det}(D, R, S, P, B) = f[S_{src}(D, R, B), \sigma_S(D, R, S, B), n_e(D, R, P, B), \mathbf{B}_0(D, R, P, B)], \quad (53)$$

The automation of a large set of simulations is possible identifying the dependence of each variable on the main variables, D, R, S, P and B , and creating the necessary lists of combinations to the creation of the simulation scripts and the production of all the simulation models.

3.3. Automating the simulations

3.3.1. Dependence of the problem variables on the main variables

Following are the dependencies of the main variables in the 3D case (where D is suppressed). The other dimensions exhibit similar dependencies. For the sake of simplification, the D' - R' - S' - P' - B' indices are omitted from the variables throughout the remainder of this paper. The coordinates of the ROI are functions of R ,

$$(x_i, x_f, y_i, y_f, z_i, z_f) = f[R]. \quad (54)$$

The minimum and maximum frequencies of the band and the grid frequency depend on the source,

$$(f_{min}, f_{max}, f_0) = f[B]. \quad (55)$$

The conductivity function is a function of S ,

$$\sigma(x, y, z) = f[S]. \quad (56)$$

The emission and the detection also,

$$(x_{src}, y_{src}, z_{src}, x_{det}, y_{det}, z_{det}) = f[S]. \quad (57)$$

The plasma density and magnetic field are functions of P ,

$$n_e(x, y, z) = f[P], \quad (58)$$

$$B_0(x, y, z) = f[P]. \quad (59)$$

Some input variables, such as the number of iterations (N_{it}), or even the FDTD parameters N_λ and N_T , can be associated with a combination of multiple main variables. In such cases, the choice is made based on convenience. Sometimes, it is useful to define the number of iterations depending on the simulated grid and plasma. Therefore, it is convenient to assume that

$$N_{it} = f[D, R, S, P, B]. \quad (60)$$

The grid resolution can be associated with only the source since it is typically a fixed parameter for most of the simulations. Therefore:

$$(N_\lambda, N_T) = f[B]. \quad (61)$$

The discussed variables represent groups of input data, and other variables in the problem depend on them. The spatial and temporal discretisation steps are given by:

$$\Delta x = \frac{c}{N_\lambda[B]f_0[B]} = f[B], \quad (62)$$

$$\Delta t = \frac{1}{N_T[B]f_0[B]} = f[B], \quad (63)$$

and the grid dimensions,

$$N_{[x,y,z]} = \frac{(x, y, z)_f[R] - (x, y, z)_i[R]}{\Delta x[B]} = f[R, B]. \quad (64)$$

The metallic structure model depends on the continuous σ function, on the region of interest and on the grid properties calculated with the band,

$$\sigma(i, j, k) = f[R, S, B], \quad (65)$$

as well as the coordinates of the excitation and detection points,

$$(i_{src}, j_{src}, k_{src}) = x_{src}/\Delta x = f[R, S, B] \quad (66)$$

$$(i_{det}, j_{det}, k_{det}) = (x_{det}, y_{det}, z_{det})/\Delta x = f[R, S, B]. \quad (67)$$

The result of each division by Δx is rounded to the integer. The plasma model depends on the continuous model of the density and magnetic field, but also on the region of interest and on the grid properties,

$$n_e(i, j, k) = f[R, P, B], \quad (68)$$

$$B_0(i, j, k) = f[R, P, B]. \quad (69)$$

All the other problem variables associated to the simulations can be written In the same way.

3.3.2. Defining the input data and generating the simulation lists

A simplified way to organize the input data dependent on a single main variable is in the form of tables/lists. These tables would contain the input variables of the problem as columns, with each row representing a different value of the main variable. The structure would be as follows:

	Main variable i	flag	$a_1[i]$...	$a_n[i]$	
$L_i =$	Value/identifier [$i = 1$]	0/1	$a_1[i = 1]$...	$a_n[i = 1]$	
	Value/identifier [$i = 2$]	0/1	$a_1[i = 2]$...	$a_n[i = 2]$	
	Value/identifier [$i = \dots$]	0/1	$a_1[i = \dots]$...	$a_n[i = \dots]$	
	Value/identifier [$i = N_i$]	0/1	$a_1[i = N_i]$...	$a_n[i = N_i]$	(70)

A string is used as an identifier for each value of the main variable (first column). A flag (second column) is used to activate or deactivate the corresponding line (1/0). This flag is particularly useful for testing purposes. The remaining columns correspond to input variables that are directly dependent on the main variable i (a_1, \dots, a_n). For example, if the main variable is R , the variables in question can represent the coordinates of the ROI, or the coordinates of the ROI in another frame of reference. In addition, there are other lists of input data that are necessary to define the variables of the problem that depend on multiple main variables. Separate lists are needed for each combination of main variables ($D-R-P-B$, $D-S-P-B$, etc). One solution to simplify this problem is to define only one list, where, in general, all the input variables have the dependence of the five main variables. This list, refereed as L_0 , has the form:

	Variable	Default value	Excep.[1]	Value[1]	...	Excep.[n]	Value[n]	
$L_0 =$	a [1]	VAL ₁	STR[1]	Value[1]	...	STR[n]	Value[n]	
	
	a [n]	VAL _n	STR[1]	Value[1]	...	STR[n]	Value[n]	(71)

Each line corresponds to a different variable. The second column represents its default value. Exceptions to the default values are indicated using a string format: D[...R[...S[...P[...B[...]]] indicating D-R-S-P-B combinations that are exceptions and the respective exception value. The argument of each main variable contains the elements to be considered in a particular independent set with all possible combinations. A predefined string can be used to indicate that all elements of a main variable should be included, simplifying the definition of dependencies for many studies. To handle the complexity arising from mixing variables of different dimensions, it is recommended to split the input into three separate datasets, one for each dimension.

A list of the $D-R-S-P-B$ combinations, denoted as L_D , is then required to create the simulations list. All the necessary lists of combinations can be derived from it. Each line contains a strings with the same format as used to define exceptions, but now they represent the possible $D-R-S-P-B$ combinations for the simulations. For example, in the simulation of 100 reflectometers with the same antenna for all the defined plasmas and bands for two dimension simulations, the list of combinations can be written in one single line as: D[2D]R[ALL]S[ALL]P[ALL]B[ALL]. Here, the string ALL represents all the existing main variable values. If a 3D simulation is also required but only for two reflectometers and one plasma, a new string is added to the L_D list.

A list of definitions related to REFMUL* (referred to as L_{RF}) and another list for computer parameters (denoted as L_H) are also necessary. These lists create different computer profiles, useful for local tests or running simulations on High-Performance Computing (HPC) systems. By changing the necessary parameters, scripts can be generated and executed on the respective computer profile. Since defining the geometry of the metallic structure or plasma involves the definition of many variables (e.g., geometry, CAD model, geometry parameters, plasma displacement, turbulence level, etc.), it is helpful to define some input variables in a separate file. The lists L_S and L_P include a variable that points to these configuration files. To summarize, the input definition process is simplified by five independent

datasets: (i) The main lists: L_R, L_S, L_P, L_B, L_0 ; (ii) the list of combinations: L_D ; (iii) the secondary lists: L_{RF}, L_H ; (iv) the structure configuration files; and the (v) the plasma configuration files.

3.3.3. Simulation scripts

The main script reads the input data and creates a directory (SD) that contains all the necessary information to run the simulations and analyze the data. This process is divided into different phases. In the first phase, the input variables are declared. Examples of these variables include the project name, input data directory, output directory, number of simulations per script file, etc. In the second phase, the lists containing all possible combinations of main variables are generated and saved in the SD directory for easy access. The list of simulations, denoted as L_{SIM} , encompasses all the combinations of $D-R-S-P-B$. Each combination represents a simulation of a setup, band and plasma, and a unique number from 1 to N_{SIM} is assigned to each combination as the simulation number. This simplifies the handling of script/function arguments. The list of metallic structures, L_{STR} includes all the combinations of $D-R-S-B$, while the list of plasmas, L_{PLS} , includes all the combinations of $D-R-P-B$. Additionally, there is a list of $D-R-S-P$ variables, denoted as L_{SP} , which represents the combinations of plasmas and metallic structures.

In many cases, it is necessary to obtain all the combinations of a list excluding the ones where the plasma model corresponds to vacuum. To facilitate this, it is useful to define a default element for vacuum, such as $P=VAC$. A modified list L^* is obtained by removing the elements with $P=VAC$, while a list consisting only of elements with $P=VAC$ is denoted as L^{**} . In this phase, the lists $L_{SIM}^*, L_{PLS}^*, L_P^*, L_{SP}^*, L_{SIM}^{**}, L_{PLS}^{**}, L_{PLS}^{**}, L_{SP}^{**}$ are also generated. For example, if the objective is to run simulations only with vacuum to test the metallic structure models, only the simulations corresponding to each combination in L_{SIM}^{**} are selected. Another important list is the list of sources, denoted as L_{SRC} , which contains the necessary source parameters for creating the reference signals. The subsequent phase involves the production of the antenna setup and plasma models. This is done by reading each combination of $D-R-S-B$ from the L_{STR} list and using a function F_S in the following format:

$$[\sigma_S(i, j, k), \text{structure arguments, other outputs}] = F_S(D, R, S, B, \text{other inputs}) \quad (72)$$

to produce the models in a for loop. The output of the function F_S consists of the σ_S tensor, whose dimensions depend on D , and the necessary arguments to run a simulation with this model in REFMUL* (such as source parameters, reference geometry points, etc.). Additionally, other output files that might be useful for other operations, such as geometry lines for plotting the model later, are also generated.

For a large number of simulations, generating and storing output data for each $D-R-S-B$ combination can be memory-intensive, especially for 3D simulations. One approach to this issue is to generate the models dynamically at the beginning of each simulation. In this case, the output of the function F_S would only include the necessary information required to generate the model at the start of the simulation. The production of the plasma works exactly in the same way, but for the combinations in the L_{PLS} list. A function F_P in the form

$$[n_e(i, j, k), \mathbf{B}_0(i, j, k), \text{plasma arguments, other outputs}] = F_P(D, R, P, B, \text{other inputs}) \quad (73)$$

runs over each $D-R-P-B$ combination and generates the plasma models accordingly. It is worth noting that the plasma tensor typically requires more memory space compared to the metallic structure models. To address memory constraints, especially for a large number of simulations or 3D simulations, a dynamic creation of the plasma model is also useful. By maintaining the structure of the input and output of the F_{STR} and F_{PLS} functions, it is possible to modify their contents without affecting the other phases of the process. This flexibility allows different users to define their own F_{STR} functions based on their specific requirements, while keeping the rest of the framework code intact. The final phase involves the creation of simulation scripts. The UTS scripts execute the simulations required to measure the UTS impulsive response. Each UTS simulation is associated with an element from the L_{STR} list. Since the sources are assumed to be independent, these simulations can be run in parallel. The MCAL scripts run simulations for calibrating the group delay within the antenna setup corresponding to each element in the L_{STR} list. The PLS scripts execute simulations with the plasma models associated with the combinations in the L_{SIM} list. The SRC scripts generate synthetic reference signals for each combination in the L_{SRC} list. This includes creating phase-shifted signals for IQ detection. To handle a large number of simulations in high-performance computing (HPC) environments, the scripts execute simulations in intervals of indices, facilitating efficient management and execution.

After the simulation script creation phase, verification scripts are also generated. These scripts include routines to

check if the simulations have completed successfully. Once this phase is completed, the required REFNUM versions and other optional files are copied to the simulation directory. Compilation scripts are generated for the various routines and REFNUM versions, with the corresponding definitions associated with the computer profile. The simulations are obtained by running the compilation scripts followed by the simulation scripts.

3.4. Producing realistic antenna setup and plasma models

The reflectometry simulation involves creating realistic plasma and antenna setup models within a specified region of interest (ROI). The ROI is defined as a rectangular parallelepiped in the simulation frame, denoted as S_0 . It is defined by two points, (x_i, y_i, z_i) and (x_f, y_f, z_f) , which represent the coordinates of the initial and final corners. In the simulation frame, the x-axis is perpendicular to the excitation plane, which corresponds to the y-z plane. In many applications, the system geometry or plasma parameters are defined in a machine frame of reference, denoted as S_m . When working with coordinates in this frame, it becomes necessary to perform coordinate transformations for various operations such as creating models, calculating positions, and plotting. Figure 5 illustrates the representation of the ROI and the coordinate system transformation.

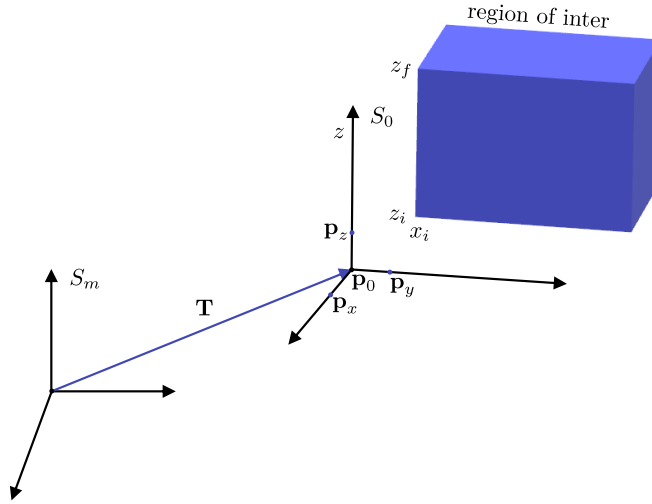


Fig. 5: Illustration of the ROI associated coordinate systems.

Since the REFNUM family of codes operates in Cartesian coordinates and the models are typically defined using Cartesian coordinates, the coordinate transformation involves a translation \mathbf{T} and a rotation matrix \mathbf{R} . Additional transformations may be required for other coordinate systems. Let $\mathbf{p}_0 = (p_{0x}, p_{0y}, p_{0z})$ be a point defined in the S_0 frame of reference. Its coordinates in the machine frame of reference S_m are obtained applying the transformation:

$$\mathbf{p}_m = (p_{mx}, p_{my}, p_{mz}) = \mathbf{T} + \mathbf{R}\mathbf{p}_0 \quad (74)$$

If the coordinates are given in S_m , the point \mathbf{p}_0 in the S_0 frame of reference can be obtained through the inverse operation: $\mathbf{p}_0 = \mathbf{R}^{-1}(\mathbf{p}_m - \mathbf{T})$. The S_0 frame of reference is defined in terms of an origin \mathbf{p}_0 and three points along each axis: \mathbf{p}_x , \mathbf{p}_y , and \mathbf{p}_z . These points can be easily determined using CAD software. Therefore, it is useful to express the translation vector \mathbf{T} and the rotation matrix \mathbf{R} in terms of these points. The translation vector is given by the origin of S_0 , which can be expressed as:

$$\mathbf{T} = \mathbf{p}_0 = (p_{0x}, p_{0y}, p_{0z}), \quad (75)$$

The unit vectors corresponding to the three axis of S_0 are given by

$$\mathbf{v}_{[x,y,z]} = \frac{\mathbf{p}_{[x,y,z]} - \mathbf{p}_0}{\sqrt{|\mathbf{p}_{[x,y,z]} - \mathbf{p}_0|^2}}, \quad (76)$$

and the \mathbf{R} matrix is given by

$$\mathbf{R} = \begin{bmatrix} R_{xx} & R_{xy} & R_{xz} \\ R_{yx} & R_{yy} & R_{yz} \\ R_{zx} & R_{zy} & R_{zz} \end{bmatrix} = \begin{bmatrix} v_{xx} & v_{yx} & v_{zx} \\ v_{xy} & v_{yy} & v_{zy} \\ v_{xz} & v_{yz} & v_{zz} \end{bmatrix}. \quad (77)$$

To produce metallic structures with realistic geometry, it is necessary to verify if each point of the FDTD grid is inside the metallic material, taking into account the respective ROI coordinates. In this context, we have developed CAD2RFM, a routine that converts CAD models into FDTD grids compatible with REFMUL codes. The CAD model is initially designed in a specific coordinate frame and then converted into a tetrahedral mesh, where the condition of being a high conductivity point can be easily analyzed. The conversion process is illustrated in figure 6 using a simple antenna model.

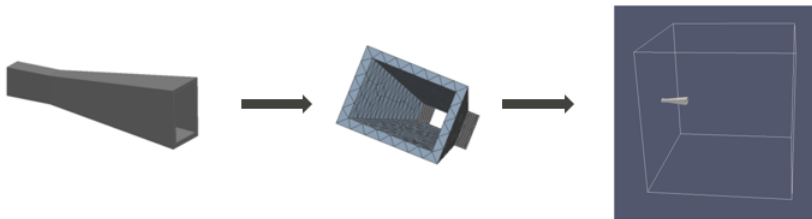


Fig. 6: The process of conversion with CAD2RFM.

The algorithm for the conversion process operates as follows:

1. The list of nodes and tetrahedrons is loaded from their respective input files.
2. If necessary, the coordinates of the nodes are converted to the simulation frame, taking into account the defined ROI.
3. The algorithm checks if each tetrahedron is inside the simulation box. If it is not inside, it is not converted. This approach allows for reading meshes of the entire machine dimension. If the tetrahedron is inside the box, the algorithm identifies the cube with the smallest volume that contains it. The indices of the cube's vertices are then calculated in the FDTD grid. As a result, there is no need to check all matrix elements.
4. Within the cube, each point is verified to determine if it lies inside the tetrahedron. If a point is inside the tetrahedron, the value of the corresponding element in the FDTD grid is modified accordingly.

The process of checking if a point p inside the cube is also inside the tetrahedron follows the algorithm:

- The tetrahedron is defined by four different nodes (p_1, p_2, p_3, p_4), which form four distinct planes: (p_1, p_2, p_3), (p_1, p_2, p_4), (p_1, p_3, p_4), and (p_2, p_3, p_4). The equation of each plane is obtained in the form $ax + by + cz + d = 0$.
- Using one of the other points of the tetrahedron, the left-hand side term of the plane equation is calculated.
- The left-hand side term is also calculated using the test point, $p = (p_x, p_y, p_z)$. If the calculated terms for both points have the same sign (positive or negative), it means they are on the same side of the plane.
- If the side is the same for all four planes, then the point p is determined to be inside the tetrahedron.

An example of an implementation in the DEMO PPR is illustrated in figure 7.

We defined the tokamak's wall using the 2D 2017 DEMO geometry with a width of 1600 mm and a thickness of 100 mm. The entire model, composed of 16 antennas, was designed using CAD software. The mesh is calculated within the coordinate frame associated with the machine. By defining the simulation frame and selecting the Region of Interest (ROI), in this case at the top of the machine (blue box), the code creates the input metallic structure for REFMUL3 (shown on the right side of the figure). Only one mesh is necessary for a system of reflectometers. The models of each reflectometer are defined by different regions of interest. The first 3D simulations with metallic structures obtained from a CAD model were performed in the study of reflectometry in the Divertor Test Tokamak, where systems of multiple detecting antennas were simulated [50, 11].

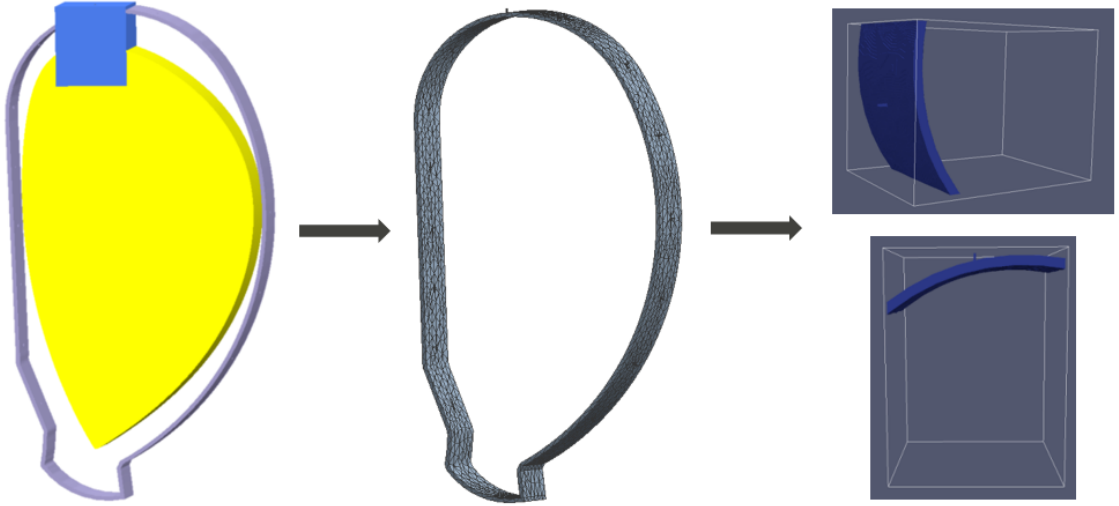


Fig. 7: Visualization of the implementation of the CAD2RFM with a 3D DEMO CAD model based on the 2D geometry from the EUROfusion official database.

A code was also developed to generate 3D plasma models from the 2D poloidal flux maps produced by the equilibrium codes. All grid points within the region of interest are converted to the Cartesian system associated with the machine. Subsequently, they are transformed into cylindrical coordinates, and the value of $\rho(R, Z)$ is calculated through interpolation. The density value is then interpolated from $n_e(\rho)$. Figure 8 illustrates different converted plasma models using the DEMO 2017 scenario.

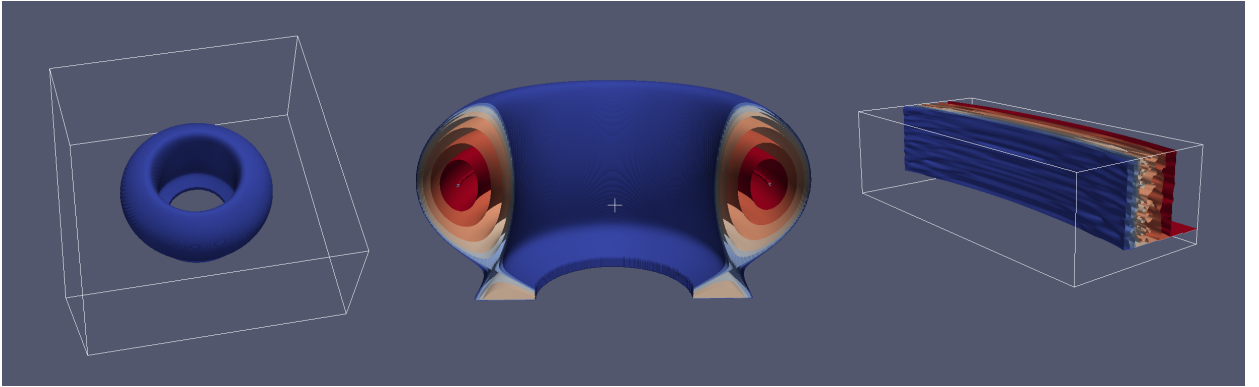


Fig. 8: Example of converted plasma models using the DEMO 2017 scenario. Full view of the DEMO plasma model (left). Central cut of the density profile (center). Example of a ROI with turbulent plasma (right).

The first model was converted into a box larger than the machine, allowing the resulting toroidal symmetry to be observed. The second model represents a cross-section, revealing different density layers. The last figure is an example of a region of interest located at the High Field Side (HFS) of the machine, with added turbulence. The code enables the displacement of the plasma in a given direction, denoted as $\mathbf{D} = (D_x, D_y, D_z)$. This can be easily implemented by applying a transformation of $-\mathbf{D}$ to the ROI coordinates before the conversion. The code can be readily adapted to accommodate a generic $n_e(R, Z)$ profile, including data from gyrokinetic simulations.

3.5. Simplifying the input data definition

In order to investigate the DEMO PPR system and demonstrate the automation of the simulations and data processing, a framework was developed based on the structure discussed in the previous sections. This framework specifically focused on the 2D O-mode case, enabling the execution of a large number of simulations. The CAD2RFM algorithm,

adapted to a 2D triangular mesh, was utilized to create an additional F_S function, which defined an array of 2D antennas with a variable setup around the DEMO wall. The DEMO 2017 geometry was employed to establish a system configuration comprising 100 reflectometers, divided into 16 regions and labeled with the code G[region][letter]. The official data from the EUROfusion database provided essential information, including the vacuum vessel geometry, the normalized poloidal flux, and the electron density profile for the baseline scenario ($R_0 = 8.938$ m, $a = 2.883$ m, and $B_0 = 4.89$ T). Due to the lack of data in the scrape-off layer region, the density profile was extrapolated using an exponential decay with a decaying length of approximately 3 cm at the equatorial zone, following the approach employed in [51]. The continuity of the density derivative was ensured, resulting in a final separatrix density of $n(\rho = 1) = 3.56 \times 10^{19} \text{m}^{-3}$, slightly lower than the input value. The resulting density map is shown in appendix C. The reflectometer configuration was determined with the probing direction aligned perpendicular to the tangent line of the separatrix, which corresponds approximately to the ideal case in the equatorial zone. For each position and configuration, the boxes to introduce the antenna setup and the corresponding regions of interest (ROI) were defined. Figure 9 illustrates the system configuration and highlights some of the regions of interest, calculated using the 2D F_S function.

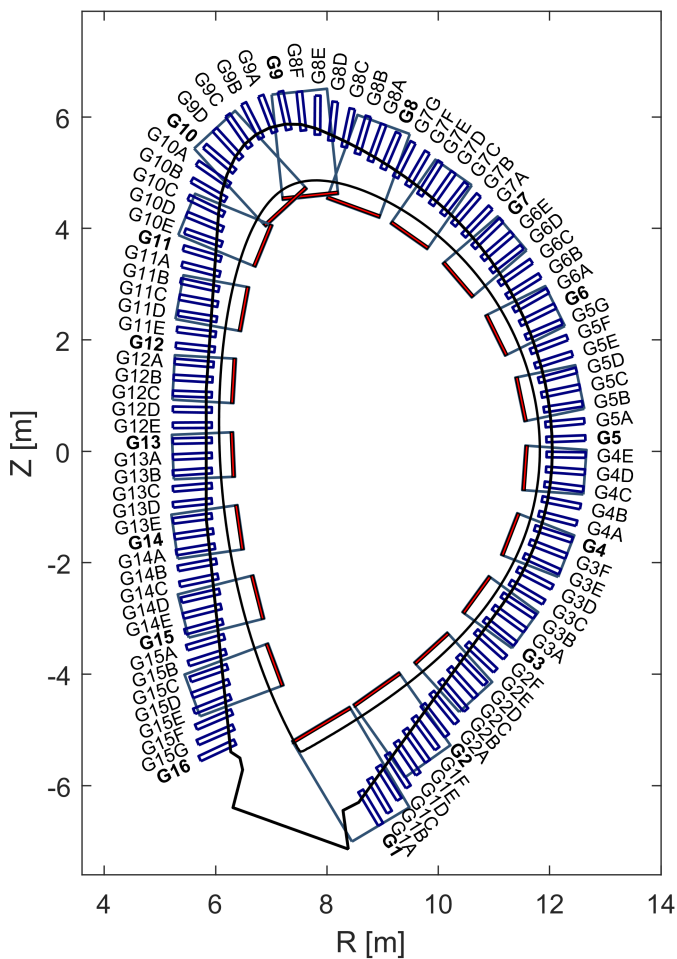


Fig. 9: Configuration of 100 reflectometers with the probing direction aligned perpendicularly to the separatrix for the DEMO 2017 model. Each reflectometer is defined by a rectangular box where the antenna model is placed. Each region of interest is defined according to the simulated scenario and takes into account the transition frame decay length (red rectangle).

The separatrix density corresponds to a probing frequency of $F_{\text{sep}} = 53.57$ GHz. The cyclotron frequency at $R_0 + a$

is $f_c = 103$ GHz, ensuring accessibility to the separatrix position. Due to the low temperature in the Scrape-off layer region (< 1 KeV), relativistic effects are not included. The selected frequency range for probing the separatrix (18-54 GHz) was divided into four bands: $K_1 = [18,29]$ GHz, $Ka_1 = [27,42]$ GHz, $Q_1 = [39,51]$ GHz, and $V_1 = [48,57]$ GHz. It is important to note that these bands do not correspond to the standard K-Ka-Q-V bands but were defined within the context of the simulations (see appendix B). The sweep is conducted over 160000 iterations, with the profiles initialized with the WKB phase derivative. Three different models were simulated for the same configuration. The first model, designed by AB, consists of the DEMO reference antenna with the blanket. This is the same model used in figure 3. The second model, designed by A, represents the DEMO reference antenna without the blanket. In the last model, designed by CAV, a 10×10 cm² cavity was implemented between the antenna and the wall surface, following the proposal from thermomechanical studies (figure 23, appendix D). With the configuration defined, the results were obtained by running the generated simulation scripts on the MARCONI computer, requiring approximately 100000 standard hours for a plasma configuration encompassing all the reflectometers and the four frequency bands.

4. Automation of the data analysis for PPR systems

4.1. Automation of the data analysis

Taking advantage of the main variables, data processing, in particular of a PPR system, can be automated for a given set of simulations. In this section we analyze the dependence of the principal variables involved in the data processing of a single measurement simulation. The lines of sight are defined by S . The density and magnetic profile along a line of sight are extracted from the input models and depend on the particular D - R - S - P - B combination,

$$[n_e(x), B_0(x)] = f[D, R, S, P, B], \quad (78)$$

where x is defined in the line of view associated with the simulated setup. The initial plasma position x_{pls} in the line of sight as well as the separatrix position where $n(x_{sep}) = n_{sep}$, have the same dependence,

$$[x_{pls}, x_{sep}(x)] = f[D, R, S, P, B]. \quad (79)$$

The reference position x_{ref} does not depend on the plasma,

$$x_{ref} = f[D, R, S, B]. \quad (80)$$

The WKB phase-shift and the group delay are calculated with $n_e(x)$ and $B_0(x)$ (equations 1-2),

$$[\varphi_{WKB}(F), \tau_{WKB}(F)] = f[D, R, S, P, B]. \quad (81)$$

In practice, the results are approximately the same for the same D - R - S - P combination. If all the reflectometers have the same set of bands, these variables can be obtained solely from the D - R - S - P combinations, considering a selected fixed band (e.g., the band with the highest f_0 for higher grid resolution), which simplifies the entire process. These calculations are performed for a set of N_{ls} lines of sight and the group delay for different propagation modes. The group delay, relative to the propagation inside the antenna setup, is obtained from simulations with the mirror,

$$\tau_M(F) = f[D, R, S, B]. \quad (82)$$

In general, this can be calculated with N_{τ_M} different methods, for example with the SFFT or IQ detection technique reviewed in chapter 2. The measured group delay is obtained with the simulated signals,

$$\tau_m(F) = f[D, R, S, P, B]. \quad (83)$$

Similarly, this can be done with N_{τ_m} different methods. Each one can consider different mirror calibrations, lines of view, detection methods, etc. If the IQ detection is used, the relative detected amplitude can also be calculated,

$$a_{det}(F) = f[D, R, S, P, B]. \quad (84)$$

Each group delay associated to a τ_m method is joined in one full-bandwidth (FB) $\tau_{FB}(F)$ profile,

$$\tau_{FB}(F) = f[D, R, S, P]. \quad (85)$$

This operation can be performed using $N_{\tau_{FB}}$ different methods, referred to as FB methods, which include different forms of initialization. The relative FB detected amplitude is also calculated.

$$a_{FB}(F) = f[D, R, S, P]. \quad (86)$$

The relative position $r(F)$ is calculated for each FB method,

$$r(F) = f[D, R, S, P]. \quad (87)$$

The position error is calculated for each line of view and for each FB method,

$$e(F) = f[D, R, S, P]. \quad (88)$$

During the entire process, the only step that is not automated is the selection of some input parameters for the IQ and SFFT detection techniques to determine the group delay. In the SFFT technique, the user specifies the lag of the detected signal, the cutoff frequency of a low-pass filter applied to the beating signal, and the spectrogram parameters. This method cannot be used to optimize the amplitude of the detected signal. In the IQ technique, the user specifies the lag of the detected signal and the cutoff frequency of a low-pass filter applied to the I and Q signals. The cutoff frequency is typically applied after the characteristic peak resulting from the plasma propagation. The higher frequency components are removed, resulting in smoother phase derivative profiles. This method is less sensitive to local fluctuations in the phase derivative and allows for the calculation of the detected amplitude.

If it is possible to automate the selection of the input parameters, particularly in the IQ method where the detected amplitude can be calculated, the statistical study of different plasmas/reflectometer configurations can be fully automated. The automation of this process is of crucial interest to reflectometry research. In this section, an automated version of the IQ detection algorithm is developed and tested to address this problem.

4.2. Automation of the signal time lag detection

Both the IQ and SFFT methods require the determination of the signal time lag. This can be achieved by comparing the signal at the source with the detected signal and identifying the point where its amplitude exceeds the noise level. Figure 10 illustrates the detected signal ($S_{det}(t)$ signal) and the beating signal at the source position ($S_{beat}(t)$ signal), along with their respective lag times. The signals in the figure correspond to the simulation with the A-setup in gap G13, for the Q_1 band, and have been decimated by a factor of 10.

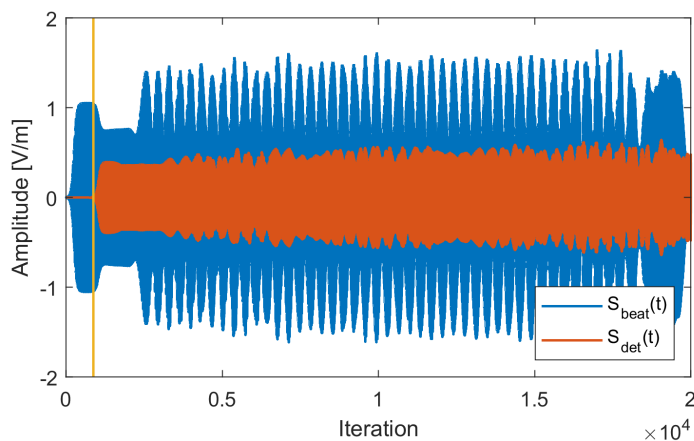


Fig. 10: Detected amplitude ($S_{det}(t)$ signal) and the beating signal at the source position ($S_{beat}(t)$ signal), before the UTS position, with the respective lag. The signals correspond to the simulation with the antenna-setup (A) in gap G13, for the Q_1 band.

One way to automate the process of lag selection is by using cross-correlation. The signal time lag can be determined by finding the displacement parameter at which the cross-correlation is maximum. Figure 11 shows the cross-correlation of the signals shown in figure 10, where the maximum at the signal lag can be observed. The lag is given in terms of the number of iterations.

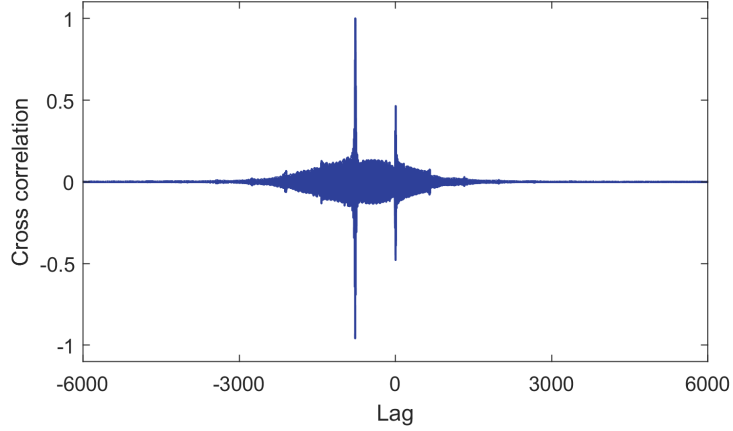


Fig. 11: The cross-correlation of the $S_{det}(t)$ and $S_{beat}(t)$ signals shown in figure 10.

Although this technique is effective for most signals in the situations of interest, there are cases where the lag time is incorrectly calculated. This typically occurs when spurious signals from reflections have considerable amplitude compared to the component from the plasma propagation. If left uncorrected, this introduces errors in the final measurement. To minimize this error, it is necessary to increase the number of simulated iterations.

4.3. Automation of the IQ detection technique

If the time lag is calculated using cross-correlation, the IQ technique can be fully automated if the filter cutoff frequency can be selected based on certain criteria. A typical I/Q signal exhibits a spectrum with a characteristic frequency corresponding to the reflection in the plasma, followed by additional high-frequency components associated with spurious signals from reflections. Figure 12 shows the spectrum of the Q_1 band Q signal, the Q-spectrum, and the filtered spectrum with a normalized cutoff frequency of $f_c = 0.02$ for the cavity setup.

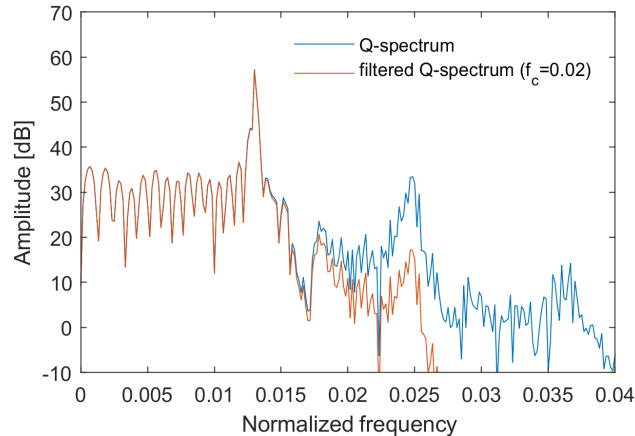


Fig. 12: The Q-spectrum of the example signal (blue) and the filtered spectrum (red) for $f_c = 0.02$.

As the cutoff frequency f_c is scanned, four distinct regimes of phase derivative profiles are observed for a given density profile. In the first one, for very low cutoff frequencies, there are not enough frequency components in the

spectrum to form a smooth phase derivative profile. The phase derivative profile approaches zero (first region). As the cutoff frequency is increased (second region), the phase derivative profile is characterized by multiple oscillations with an increasing mean value. In the third region, which is of particular interest, the characteristic peak is included, resulting in a smooth phase derivative profile. In the fourth region, when higher frequencies are included in the I/Q-spectrum, the smoothness of the phase derivative profile is disrupted by increasing perturbations. The third region is characterized by a local minimum of the the standard deviation of the phase derivative, $\sigma(\partial\varphi/\partial f)$, when the cutoff frequency is swept. The selected cutoff frequency, f_{c0} , corresponds to the cutoff frequency at this minimum point. In the first and second regions, the standard deviation increases as the principal spectrum components are added. Conversely, in the fourth region, the standard deviation increases as the higher frequencies associated with the spurious signals are included. The standard deviation of the sum of two functions, f_1 and f_2 , is calculated as follows:

$$\sigma^2(f_1 + f_2) = \sigma^2(f_1) + \sigma^2(f_2) + 2[\langle f_1 f_2 \rangle - \langle f_1 \rangle \langle f_2 \rangle], \quad (89)$$

where $\langle \dots \rangle$ is the mean value. If f_1 is a smooth phase derivative associated to a characteristic peak and f_2 is the component introduced by increasing the cutoff frequency, the condition $\sigma(f_1 + f_2) > \sigma(f_1)$ is satisfied if

$$\langle f_1 f_2 \rangle - \langle f_1 \rangle \langle f_2 \rangle > -\frac{\sigma^2(f_2)}{2}. \quad (90)$$

If f_1 is a positive constant, this condition is always satisfied if $\sigma(f_2) > 0$. For a slowly varying positive phase derivative profile f_1 and a noise-like f_2 function, this condition is still being met. Dividing the frequency range Δf in N intervals of width $\Delta f'$ labeled with the i index and taking constant the values of f_1 in each interval, c_i , we get

$$\langle f_1 f_2 \rangle = \frac{\int_{\Delta f} f_1 f_2 df}{\Delta f} \approx \sum_i^N \left(\frac{c_i}{\Delta f} \right) \int_{\Delta f'_i} f_2 df \quad (91)$$

Assuming uncorrelated noise-like functions where $\int_{\Delta f} f_2 df \approx N \int_{\Delta f'_i} f_2 df$,

$$\langle f_1 \rangle \langle f_2 \rangle = \frac{\int_{\Delta f} f_1 df}{\Delta f} \frac{\int_{\Delta f} f_2 df}{\Delta f} = \sum_i^N \left(\frac{c_i}{\Delta f} \right) \left(\frac{\int_{\Delta f} f_2 df}{N} \right) \approx \sum_i^N \left(\frac{c_i}{\Delta f} \right) \int_{\Delta f'_i} f_2 df. \quad (92)$$

Thus, $\langle f_1 f_2 \rangle \approx \langle f_1 \rangle \langle f_2 \rangle$ and the left side of equation (90) is approximately zero. This demonstrates that the minimum standard deviation of the phase derivative is a good selection criteria for the type of signals that are expected.

4.3.1. Testing the principle in a simulation with mirror

Figure 13 shows the standard deviation as a function of the normalized cutoff frequency of the fourth order high pass Butterworth filter applied to the I/Q signals, corresponding to the Q_1 band of gap G13 with the blanket removed.

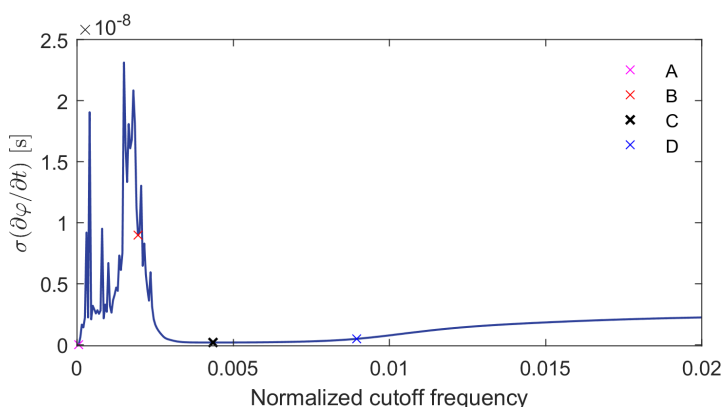


Fig. 13: The standard deviation of the phase derivative as a function of the normalized cutoff for the Q_1 band signal of the gap G13 (wall removed).

Throughout this work, the applied normalized cutoff frequency is also referred by cutoff frequency, different from the plasma cutoff frequency. The phase derivative profiles associated with points A ($f_c = 0$), B ($f_c < f_{c0}$), C ($f_c = f_{c0}$) and D ($f_c > f_{c0}$) are shown in figure 14, associated respectively to the four regions.

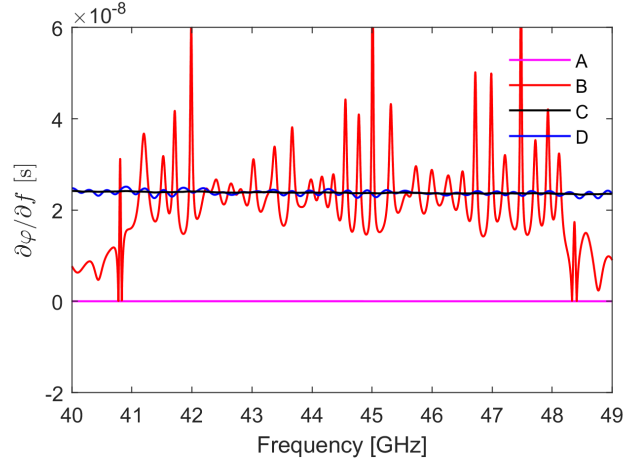


Fig. 14: Phase derivative profile associated with the points A ($f_c = 0$), B ($f_c < f_{c0}$), C ($f_c = f_{c0}$) and D ($f_c > f_{c0}$).

Since for lower cutoff frequencies the standard deviation is also lower, the minimum standard deviation condition is not sufficient to select the optimal cutoff frequency. One possibility is to use the position of the maximum standard deviation to determine the minimum cutoff frequency value, denoted as f_{c0} , where the minimum standard deviation occurs. However, depending on the case and the limit of the cutoff frequency being used for the sweep, it is not guaranteed that the maximum standard deviation occurs before f_{c0} . This issue is addressed by evaluating the derivative of the mean phase derivative profile with respect to the cutoff frequency. Figure 15 illustrates the mean phase derivative as a function of the cutoff frequency and its derivative for the considered signal.

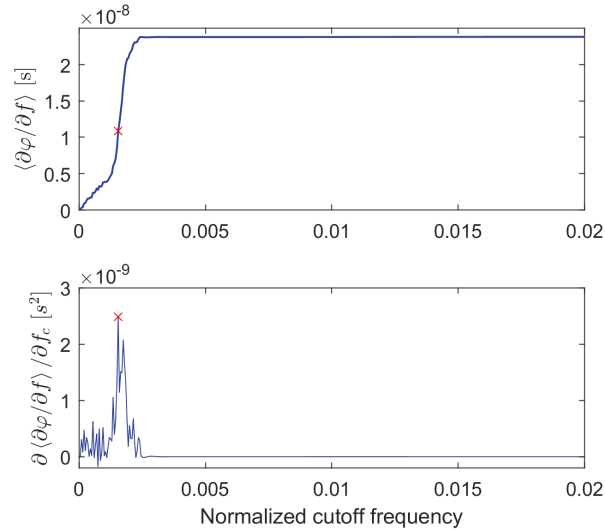


Fig. 15: Mean phase derivative as function of the cutoff frequency and its derivative for the considered signals. The red point corresponds to the derivative maximum.

The mean phase derivative initially increases with the cutoff frequencies, resulting in the formation of a smooth profile. Once the characteristic peak is included, the mean phase derivative stabilizes. Even if additional frequencies are added to the spectrum, the mean phase derivative tends to increase gradually. Therefore, the position of the maximum of its derivative can be used as criteria to determine $f_{c,min}$.

The procedure for estimating the group delay can be summarized in five steps:

- The time-lag is calculated with the cross correlation.
- The standard deviation of the phase derivative as function of f_c is calculated,

$$s(f_c) = \sigma\left(\frac{\partial\varphi}{\partial f}\right) \quad (93)$$

- The mean $m(f_c)$ of the phase derivative and its derivative $d(f_c)$ are given by

$$m(f_c) = \left\langle \frac{\partial\varphi}{\partial f} \right\rangle \quad (94)$$

$$d(f_c) = \frac{\partial}{\partial f_c} \left\langle \frac{\partial\varphi}{\partial f} \right\rangle \quad (95)$$

- The cutoff frequency of the maximum of $d(f_c)$ is selected, $f_{c \min}$.
- The selected cutoff frequency to filter the I/Q signals, f_{c0} , is determined by the cutoff frequency associated to the minimum standard deviation after $f_{c \min}$.

4.3.2. Simulation with the plasma

Figure 16 (a) shows the phase derivative standard deviation and the mean for the three different setups (A - antenna, AB - antenna with blanket, CAV - 10 cm cavity), for the Q_1 band. The selected points with the minimum standard deviation are also represented. The phase derivative values are calculated using the same reference, which explains why the mean is approximately the same for all configurations at higher cutoff frequencies. However, the source position is different for the CAV configuration, resulting in a difference at lower cutoff frequencies. The standard deviation in region four, where higher frequency components are added, serves as a measure of the impact of geometry on noise detection. In this case, the A configuration has the lowest value due to the absence of a blanket, while the AB configuration exhibits a higher noise level because the 10 cm cavity reduces plasma-wall reflections by a factor.

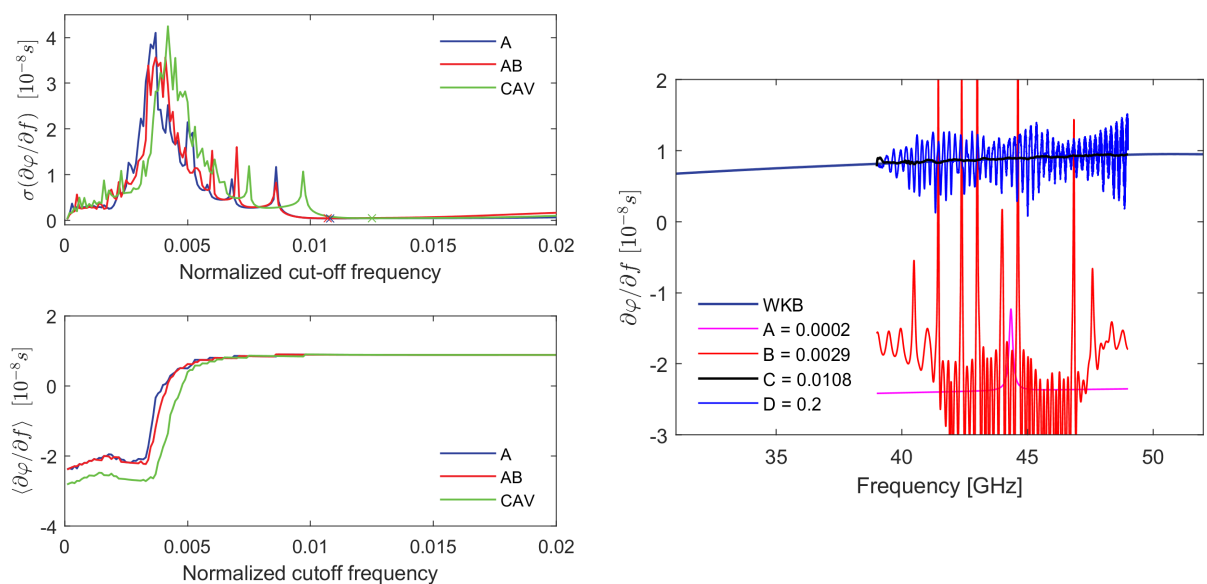
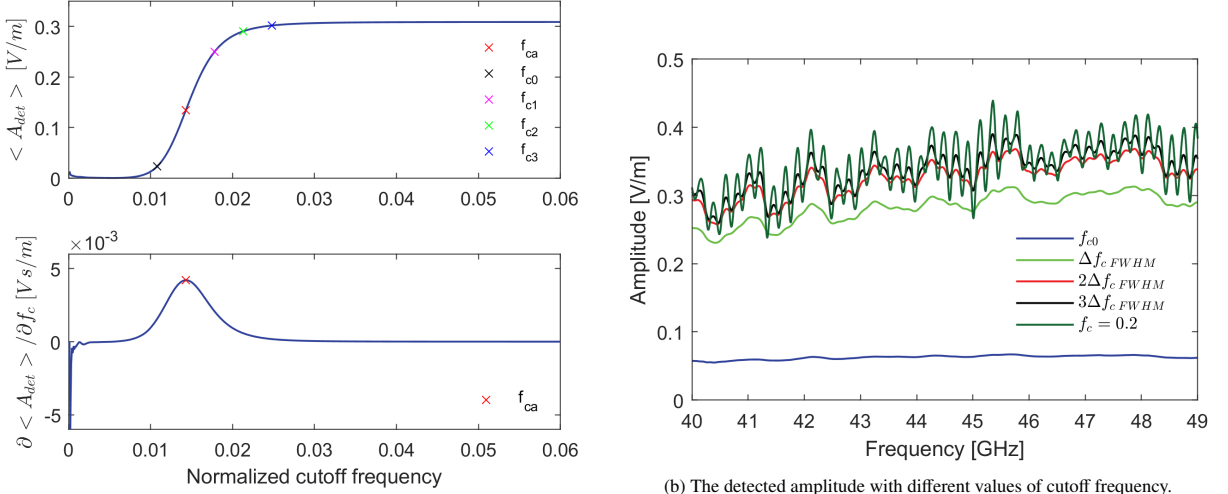


Fig. 16: (a) The standard deviation and the mean for the three different setups (A - antenna, AB - antenna with blanket, CAV - 10 cm cavity). (b) Phase derivative profiles for different values of cutoff frequency in the case of the setup with the blanket removed.

In simulations involving the plasma, the term corresponding to the setup propagation is subtracted from the phase derivative. When the filter cutoff frequency is set to zero, the mean of the phase derivative is negative and the standard deviation is low. In contrast to simulations with the mirror, the cutoff frequency can be selected based on the frequency of the minimum standard deviation, denoted as $s(f_c)$, if the derivative of the mean phase derivative, denoted as $m(f_c)$, is greater than zero. Figure 16 (b) illustrates the phase derivative profiles for different cutoff frequency values in the case of the A setup, showcasing the different phases of the filtering process. Only the data from the 40-50 GHz frequency range was utilized to determine $s(f_c)$ and $m(f_c)$.

The detected amplitude, denoted as $A_{det}(f) = 2\sqrt{Q^2(f) + I^2(f)}$, also depends on the applied cutoff frequency. Figure 17 (a) displays the mean detected power and its derivative for this particular example.



(a) The mean detected power $\langle A_{det}(f) \rangle$ and its derivative.

(b) The detected amplitude with different values of cutoff frequency.

Fig. 17: (a) The mean detected power $\langle A_{det}(f) \rangle$ and its derivative. (b) The detected amplitude with different values of cutoff frequency.

As the cutoff frequency increases to values above the characteristic frequency, the level of amplitude stabilizes. Its derivative has a maximum in this transition, and its positive part has a Gaussian-like shape. The frequency of this maximum, f_{ca} , is, in general, slightly different from the cutoff frequency selected for phase derivative calculation, f_{c0} . Figure 17 (b) shows the detected amplitude for different cutoff frequencies, including multiples of the full width at half maximum ($\Delta f_{c, FWHM}$),

$$f_{cn} = f_{ca} + n\Delta f_{c, FWHM}. \quad (96)$$

When the spurious components are included, the $a_{det}(f)$ profile can be viewed as the sum of a smooth profile and fluctuations. The f_{c2} or f_{c3} frequencies are ideal to compute smooth amplitude profiles.

4.4. Comparison of the results with the manual data analysis

The automated IQ algorithm (IQA) was applied to data from the 100 reflectometers positioned at different locations in the machine. The results were compared with those obtained using manual lag time and frequency selection (IQ). The fit parameters of the waveguide propagation function can be found in appendix E, specifically in figures 24a (A model) and 24 (CAV model). It can be observed that both parameters remain nearly constant across different reflectometers, as the only difference lies in the connection with the blanket due to the varying emitting angle. The comparison between the IQA algorithm and manual selection shows a low error in the calculated parameters for the different setups. In simulations with the mirror, the correlation method usually provides an accurate estimation of the signal lag, as the amplitude of the characteristic frequency is always higher than possible wall-mirror reflections. The position error is shown in figure 18 (a) for the antenna setup without a blanket (A) and in figure 18 (b) for the setup with the 10 cm cavity (CAV) for both techniques.

For the configuration without the blanket (A), the signal lag estimation using cross-correlation is accurate because the plasma-wall reflections are eliminated and the characteristic frequency due to plasma propagation is well-defined, as observed in the spectrum of figure 12. The IQA algorithm successfully selects similar frequencies to the manual

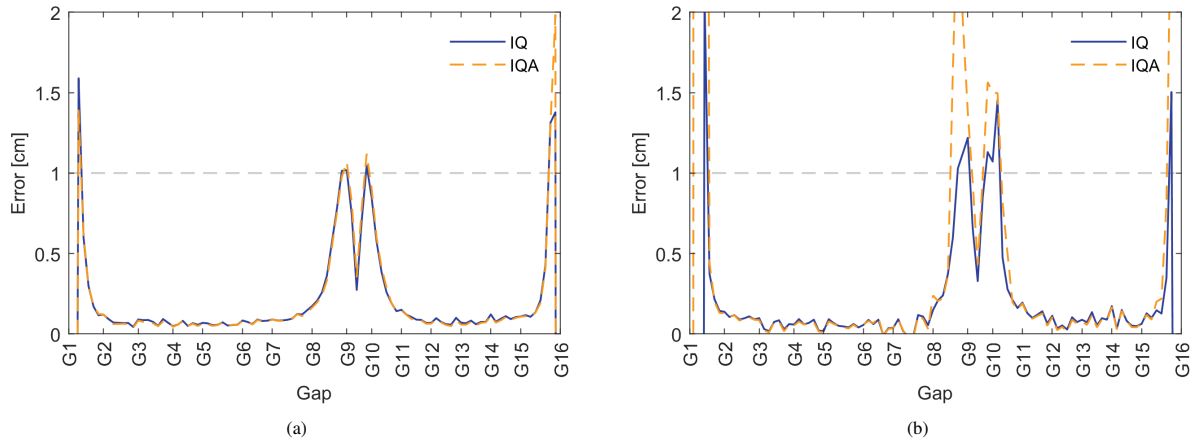


Fig. 18: (a) The position error calculated with the IQ and IQA methods for the A setup. (b) The position error calculated with the IQ and IQA techniques for the CAV setup.

selection in almost all gaps, including the divertor and top of the machine regions, where the error is slightly higher due to the divergence of flux lines or signal loss. In the CAV configuration, the results are similar in gaps G1D-G8C and G10D-G15C, where the characteristic frequency is well-defined despite the presence of plasma-wall reflection components (similar to Figure 12 with higher amplitude secondary peaks). However, in the divertor and top of the machine regions, there is a significant difference in the results. This is primarily due to incorrect lag calculation and difficulties in filtering the signal caused by power losses in the 18-40 GHz range, as revealed in the power losses analysis. In these regions, the relative amplitude of the characteristic frequencies is comparable to that of the plasma-wall reflections, and the flux lines are not approximately parallel to the separatrix line. Reflectometer configurations that exhibit these effects are not ideal for measurements and should be optimized to maximize the detected signal amplitude. Regardless of that, the IQA algorithm is capable of effectively filtering the signals and accurately determining the position error in the cases of interest.

Figure 19 illustrates the averaged power losses between the emission and detection ($P_l = -20 \log_{10} \langle A_{det}/A_{src} \rangle$) in the 50-54 GHz range (separatrix region) for both setups and in the 18-19 GHz range for the CAV setup, calculated with f_{c2} .

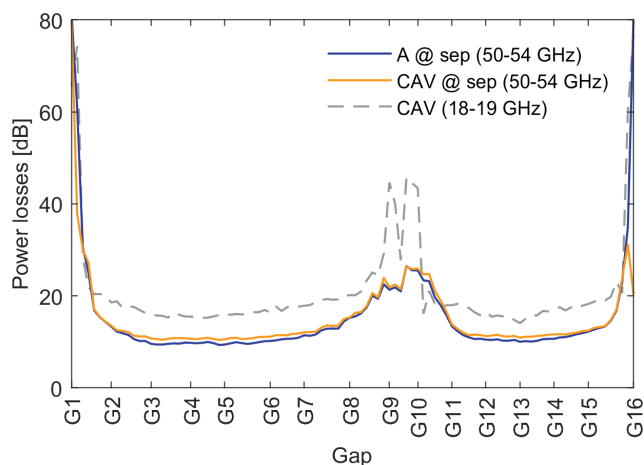


Fig. 19: The mean detected power losses for the different possible setups.

The results reveal power losses on the order of 10-15 dB in the equatorial zone and 15-30 dB at the top of the machine, which aligns with the lower plasma-wall distance in the equatorial region and corresponds to the order of

values observed in experiments [52]. In the equatorial region, where the perpendicular alignment between the probing beam direction and the separatrix line is favorable, conditions similar to the ideal plasma model can be achieved, leading to reduced error and power losses resulting from beam divergence and propagation.

In the divertor region (G1-G1C and G15C-G16), no characteristic components associated with propagation are observed since the signal is predominantly lost. The interpretation of the value returned by the IQA algorithm in these regions is nontrivial and not of interest. The higher power losses observed at G8C-G10 for the lower frequencies explains the difficulties encountered in determining the position error using the developed techniques (figure 18 (b)). To address this issue, optimization is required, which can be achieved by sweeping the direction of the probing beam and finding a compromise in detected amplitude between the lower and higher frequencies. These results can be obtained with the application of the developed framework and data processing algorithms.

5. Conclusions

The study and design of PPR systems require numerical simulation and estimation of position error and power losses for multiple plasma and reflectometer configurations. This evaluation is necessary to assess the system's performance in terms of signal-to-noise ratio and accuracy under various conditions. The presented automation techniques address the requirements for optimizing a PPR system by running a full-wave code on a large set of configurations and processing the corresponding output signals. This methodology can also be applied to other complex systems or tasks that involve a significant number of runs, such as optimization problems or the determination of error bars.

The signals and other variables of interest in a multi-reflectometer system (MRS) were identified, and their dependencies were analyzed using indices that represent subsystems associated with groups of input data. The data analysis process for PPR systems was also reviewed using the same formalism. This enabled a comprehensive problem description and facilitated the development of a framework to simplify the simulation process for a set of multi-reflectometer systems. The synthetic signals and other variables and operations involved in the simulation process can be written as a function of a reduced number of main variables, the simulation dimension (D), region of interest (R), metallic structure (S), plasma (P), and source/band (B). This approach allows the definition of inputs through independent lists of variables, a list specifying dependencies between their elements, and configuration files on which the simulation scripts depend in a generalized form. Various solutions were proposed to generate realistic plasma/reflectometer models and minimize the complexity of input definition.

The automation of data processing in the context of PPR systems became possible through the development of an algorithm to determine the signal delay and cutoff frequency used for filtering the I/Q signals. With the principle that the optimal cutoff frequency of the high pass filter applied to the I/Q signals minimizes the standard deviation of the phase derivative/group delay profile, an automated version of the IQ detection was developed. This technique enables the extraction of the phase derivative and the detected amplitude from signals of a general simulation. The local minimum is identified after reaching a minimum cutoff frequency. This minimum cutoff frequency corresponds to the cutoff frequency of the maximum of the mean phase derivative function. In simulations involving plasma, this minimum frequency can also be obtained by identifying the cutoff frequency at which the mean phase derivative function transitions from negative to positive. The detected amplitude is determined by filtering the I/Q signals using a cutoff frequency corresponding to 1-2 times the full width at half maximum (FWHM) above the cutoff frequency of the maximum of the mean detected amplitude derivative. The developed techniques and algorithms were validated using the reference 2017 DEMO baseline scenario available in the official EUROfusion database. The results obtained from the algorithm were compared to the manual selection of the signal delay and IQ filter. In simulations without plasma-wall effects, the algorithm yielded similar results to the manual selection. However, when the wall effects were included, there were slight deviations from the results obtained through manual selection. These deviations occurred when the amplitude of the characteristic frequency of the I/Q signals was comparable to the reflections, or when the estimation of signal lag was not accurate due to losses at lower frequencies. These configurations are not of interest for measurement purposes, and the algorithm performs well for the cases of interest.

The automation techniques of the simulation process and data analysis allow a brute-force approach to reflectometry problems, being essential for the design of the future reflectometry systems. They can be used to optimize a generic PPR system for the equilibrium scenario and verify its stability under the deviations to the equilibrium that may occur during the discharge, for example plasma displacement or turbulence. The automation of the simulation process is applicable to a wide range of multi-reflectometer systems and can be utilized in simulating various applications and reflectometry techniques. With the help of the tools and data analysis methods developed in this work based

on the Ricardo's PhD thesis [53], the future of microwave reflectometry research lies in the systematic analysis of different reflectometer geometries and plasmas to study the impact of the plasma parameters in the measurements and design reflectometry systems. As computational performance continues to improve and simulation frameworks and data analysis codes are optimized and parallelized, the cost and execution time of these tasks will be reduced. This, in turn, will contribute to the advancement and research of reflectometry systems and, consequently, to the development and sustainability of thermonuclear fusion.

Acknowledgements

IPFN activities received financial support from “Fundação para a Ciência e Tecnologia” through projects UIDB/50010/2020 and UIDP/50010/2020. This work has been carried out within the framework of the EUROfusion Consortium, funded by the European Union via the Euratom Research and Training Programme (Grant Agreement No. 101052200—EUROfusion). Views and opinions expressed are, however, those of the author(s) only and do not necessarily reflect those of the European Union or the European Commission. Neither the European Union nor the European Commission can be held responsible for them.

References

- [1] E. Mazzucato, Microwave reflectometry for magnetically confined plasmas, *Review of Scientific Instruments* 69 (6) (1998) 2201. doi : <https://doi.org/10.1063/1.1149121>.
- [2] L. Vermare, S. Heuroux, F. Clairet, G. Leclert, F. da Silva, Density fluctuation measurements using x-mode fast sweep reflectometry on tore supra, *Nuclear Fusion* 46 (9) (2006) S743. doi : [10.1088/0029-5515/46/9/S10](https://doi.org/10.1088/0029-5515/46/9/S10).
- [3] A. Medvedeva, C. Bottereau, F. Clairet, P. Hennequin, U. S. G. Birkenmeier, M. C. G. Conway, T. Happel, S. Heuroux, Density profile and turbulence evolution during 1-h transition studied with the ultra-fast swept reflectometer on asdex upgrade, *Plasma Physics and Controlled Fusion* 59 (12) (2017) 125014. doi : [10.1088/1361-6587/aa9251](https://doi.org/10.1088/1361-6587/aa9251).
- [4] F. Clairet, S. Heuroux, C. Bottereau, D. Molina, L. Ducobu, F. Leroux, A. Barbuti, Fast sweeping reflectometry upgrade on tore supra, *Review of Scientific Instruments* 81 (10) (2010) 10D903. doi : [10.1063/1.3460624](https://doi.org/10.1063/1.3460624).
- [5] J. Santos, L. Guimarães, M. Zilker, W. Treutterer, M. Manso, Reflectometry-based plasma position feedback control demonstration at asdex upgrade, *Nuclear Fusion* 52 (03) (2012) 032003. doi : [DOI:10.1088/0029-5515/52/3/032003](https://doi.org/10.1088/0029-5515/52/3/032003).
- [6] J. M. Santos, G. S. Santos, M. Zilker, L. Guimarães, C. Rapson, W. Treutterer, Enhancement of the asdex upgrade real-time plasma position reflectometry diagnostic, *IEEE Transactions on Nuclear Science* 62 (2014). doi : [10.1109/RTC.2014.7097429](https://doi.org/10.1109/RTC.2014.7097429).
- [7] J. Santos, L. Guimarães, C. Rapson, G. Santos, A. Silva, W. Treutterer, M. Zilker, Real-time reflectometry - an asdex upgrade dcs plugin app for plasma position and shape feedback control, *Fusion Engineering and Design* 3 (2017) S0920379617302193. doi : [10.1109/RTC.2014.7097429](https://doi.org/10.1109/RTC.2014.7097429).
- [8] W. Biel, R. Albanese, R. Ambrosino, M. Ariola, M. Berkel, I. Bolshakova, K. Brunner, R. Cavazzana, M. Cecconello, S. Conroy, A. Dinklage, I. Duran, R. Dux, T. Eade, S. Entler, G. Ericsson, E. Fable, D. Farina, L. Figini, C. Finotti, T. Franke, L. Giacomelli, L. Giannone, W. Gonzalez, A. Hjalmarsson, M. Hron, F. Janky, A. Kallenbach, J. Kogoj, R. König, O. Kudlacek, R. Luis, A. Malaquias, O. Marchuk, G. Marchiori, M. Mattei, F. Maviglia, G. D. Masi, D. Mazon, H. Meister, K. Meyer, D. Micheletti, S. Nowak, C. Piron, A. Pironti, N. Rispoli, V. Rohde, G. Sergienko, S. E. Shawish, M. Siccino, A. Silva, F. da Silva, C. Sozzi, M. Tardocchi, M. Tokar, W. Treutterer, H. Zohm, Diagnostics for plasma control – from iter to demo, *Fusion Engineering and Design* 146 (2019) 465–472. doi : <https://doi.org/10.1016/j.fusengdes.2018.12.092>.
- [9] E. Ricardo, P. Varela, A. Silva, B. Gonçalves, Assessment and performance optimization of the iter plasma position reflectometry in-vessel oversized waveguide bends, *Fusion Engineering and Design* 7 (2015) 1593–1596. doi : <https://doi.org/10.1016/j.fusengdes.2015.06.169>.
- [10] J. Belo, P. Varela, E. Ricardo, A. Silva, P. Quental, Performance assessment of critical waveguide bends for the iter in-vessel plasma position reflectometry systems, *Fusion Engineering and Design* 123 (2017) 773–777.
- [11] J. Santos, E. Ricardo, F. da Silva, T. Ribeiro, S. Heuroux, A. Silva, Cad model input pipeline for reful3 full-wave 3d fdtd simulator, *Journal of Instrumentation* 16 (2021) C11013. doi : [10.1088/1748-0221/16/11/C11013](https://doi.org/10.1088/1748-0221/16/11/C11013).
- [12] R. Luís, R. Moutinho, L. Prior, P. B. Quental, A. Lopes, H. Policarpo, N. Velez, A. Vale, A. Silva, A. Malaquias, Nuclear and thermal analysis of a reflectometry diagnostics concept for demo, *IEEE Transactions on Plasma Science* 46 (5) (2018) 1247–1253. doi : [10.1109/TPS.2017.2780922](https://doi.org/10.1109/TPS.2017.2780922).
- [13] G. Marchiori, G. D. Masi, R. Cavazzana, A. Cenedese, N. Marconato, R. Moutinho, A. Silva, Study of a plasma boundary reconstruction method based on reflectometric measurements for control purposes, *IEEE Transactions on Plasma Science* 46 (5) (2018) 1285–1290. doi : [10.1109/TPS.2018.2797549](https://doi.org/10.1109/TPS.2018.2797549).
- [14] E. Mazzucato, Relativistic effects on microwave reflectometry, *Physics of Fluids B Plasma Physics* 4 (1992) 3460.
- [15] F. da Silva, S. Heuroux, E. Ricardo, A. Silva, T. Ribeiro, Modelling reflectometry diagnostics: finite-difference time-domain simulation of reflectometry in fusion plasmas, *Journal of Instrumentation* 14 (2019) C08003.
- [16] F. da Silva, S. Heuroux, E. Ricardo, P. Quental, J. Ferreira, Assessment of the measurement performance of the in-vessel system of gap 6 of the iter plasma position reflectometer using a finite-difference time-domain maxwell full-wave code, *Review of Scientific Instruments* 87 (11) (2016) 11E727.

- [17] A. Silva, F. da Silva, S. Heurax, B. Gonçalves, First assessment of microwave diagnostics for demo, *Fusion Engineering and Design* 96-97 (2015) 948–951.
- [18] F. da Silva, S. Heurax, E. Ricardo, A. Silva, T. Ribeiro, Benchmarking 2d against 3d ftdt codes in the assessment of reflectometry performance in fusion devices, *Journal of Instrumentation* 14 (2019) C08004.
- [19] F. da Silva, S. Heurax, E. Ricardo, A. Silva, T. Ribeiro, Modelling reflectometry diagnostics: finite-difference time-domain simulation of reflectometry in fusion plasmas, *Journal of Instrumentation* 14 (2019) C08003.
- [20] Eurofusion database, <https://ims.euro-fusion.org>.
- [21] I. H. Hutchinson, *Principles of Plasma Diagnostics*, 2nd Edition, CUP, 2005.
- [22] H.-J. Hartfuß, T. Geist, *Fusion Plasma Diagnostics with mm-Waves: An Introduction*, 1st Edition, Wiley-VCH, 2013.
- [23] H. Bottollier-Curtet, G. Ichtchenko, Microwave reflectometry with the extraordinary mode on tokamaks: Determination of the electron density profile of petula-b, *Review of Scientific Instruments* 58 (1987) 539–546. doi:<https://doi.org/10.1063/1.1139266>.
- [24] A. Silva, The asdex upgrade broadband microwave reflectometry system, Ph.D. thesis, Universidade técnica de Lisboa (2006).
- [25] J. Santos, Fast reconstruction of reflectometry density profiles on asdex upgrade for plasma position feedback purposes, Ph.D. thesis, Universidade técnica de Lisboa (2008).
- [26] B. Boashash, Estimating and interpreting the instantaneous frequency of a signal. i. fundamentals, *Proceedings of the IEEE* 80 (1992) 520–538.
- [27] B. Boashash, Estimating and interpreting the instantaneous frequency of a signal. ii. algorithms and applications, *Proceedings of the IEEE* 80 (1992) 540–568.
- [28] P. Varela, M. Manso, A. Silva, the CFN Team, the ASDEX Upgrade Team, Review of data processing techniques for density profile evaluation from broadband fm-cw reflectometry on asdex upgrade, *Nuclear Fusion* 46 (09) (2006) S693–S707. doi:[10.1088/0029-5515/46/9/S05](https://doi.org/10.1088/0029-5515/46/9/S05).
- [29] H. Zohm, *Magneto-hydrodynamic Stability of Tokamaks*, 1st Edition, Wiley-VCH, 2015.
- [30] M. C. S. Hacquin, S. Heurax, G. Leclert, Fast computations of wave propagation in an inhomogeneous plasma by a pulse compression method, *Journal of Computational Physics* 174 (2001) 1–11. doi:<https://doi.org/10.1006/jcph.2001.6867>.
- [31] R. White, F. Chen, Amplification and absorption of electromagnetic waves in overdense plasmas, *Plasma Physics* 16 (1974) 565. doi:[10.1088/0032-1028/16/7/002](https://doi.org/10.1088/0032-1028/16/7/002).
- [32] G. Cunningham, Use of the absolute phase in frequency modulated continuous wave plasma reflectometry, *Review of Scientific Instruments* 79 (2008) 083501.
- [33] C. L. J. Lips, S. Heurax, B. Plaum, On frequency-independent horn antenna design for plasma positioning reflectometers, from simulation to prototype testing, *Journal of Instrumentation* 16 (2021) P07040. doi:[doi:10.1088/1748-0221/16/07/P07040](https://doi.org/10.1088/1748-0221/16/07/P07040).
- [34] J. Santos, A. Silva, Real-time detection and correction of frequency sweeping non-linearities of fmcw reflectometry microwave sources, *Journal of Instrumentation* 14 (11) (2019) C11017–C11017.
- [35] P. Varela, M. Manso, A. Silva, J. Fernandes, F. Silva, Initialization of plasma density profiles from reflectometry, *Review of Scientific Instruments* 66 (1995) 4937. doi:<https://doi.org/10.1063/1.1146178>.
- [36] J. Santos, F. Nunes, M. Manso, I. Nunes, Neural network evaluation of reflectometry density profiles for control purposes, *The Review of scientific instruments* 70 (1998) 521–524.
- [37] R. Morales, S. Heurax, R. Sabot, S. Hacquin, F. Clairot, the Tore Supra Team, Reconstruction of hollow areas in density profiles from frequency swept reflectometry, *Plasma Science and Technology* 22 (2020) 064005.
- [38] F. da Silva, S. Heurax, M. Manso, Studies on o-mode reflectometry spectra simulations with velocity shear layer, *Nuclear Fusion* 46 (9) (2006) 816.
- [39] F. da Silva, Finite-difference time-domain simulation of reflectometry in fusion plasmas, Ph.D. thesis (2007).
- [40] F. da Silva, S. Heurax, T. Ribeiro, B. Scott, Development of a 2d full-wave je-ftdt maxwell x-mode code for reflectometry simulation, 9th International Reflectometry Workshop (IRW9) (2009).
- [41] L. Xu, N. Yuan, Ftdt formulations for scattering from 3-d anisotropic magnetized plasma objects, *IEEE Antennas and Wireless Propagation Letters* 5 (2006) 335–338.
- [42] F. da Silva, M. C. Pinto, B. Després, S. Heurax, Stable explicit coupling of the yee scheme with a linear current model in fluctuating magnetized plasmas, *Journal of Computational Physics* 295 (2015) 24–45.
- [43] A. Taflov, S. C. Hagness, *Computational Electrodynamics: The Finite-Difference Time-Domain Method*, 3rd Edition, 2005.
- [44] F. da Silva, S. Heurax, S. Hacquin, M. Manso, Unidirectional transparent signal injection in finite - difference time-domain electromagnetic codes - application to reflectometry simulations, *Journal of Computational Physics* 203 (2005) 467–492.
- [45] F. da Silva, S. Heurax, B. Després, M. C. Pinto, Numerical advances in kernels for ftdt maxwell codes using the yee algorithm in proceedings of the 11th international reflectometry, Workshop for fusion plasma diagnostics — IRW11 (2013).
- [46] Openmp website, <https://www.openmp.org>.
- [47] Mpi website, <https://www.open-mpi.org>.
- [48] E. Ricardo, F. da Silva, S. Heurax, A. Silva, On the edge turbulence effects on the density profile reconstruction using o-mode reflectometers, *Fusion Engineering and Design* 171 (2021) 112652. doi:<https://doi.org/10.1016/j.fusengdes.2021.112652>.
- [49] J. Berenger, A perfectly matched layer for the absorption of electromagnetic waves, *Journal of Computational Physics* 114 185–200.
- [50] F. da Silva, J. Ferreira, G. D. Masi, S. Heurax, E. Ricardo, T. Ribeiro, O. Tudisco, R. Cavazzana, O. D’Arcangelo, A. Silva, A first full wave simulation assessment of reflectometry for ddt, *Journal of Instrumentation* 14 (2019) C08011.
- [51] E. Ricardo, F. Silva, S. Heurax, A. Silva, On the edge turbulence effects on the density profile reconstruction using o-mode reflectometers, *Fusion Engineering and Design* 171 (2021) 112652.
- [52] Final report on deliverables (D001) Advanced simulation studies on microwave diagnostics under DEMO conditions, (D002) Advanced concept on in vessel and ex vessel components, (D003) Complete set of expected performance data of all MW diagnostics. EUROfusion IDM reference No EFDA D 2PHYUD.
- [53] E. Ricardo, Assessment of reflectometry diagnostics for demo, Ph.D. thesis, Universidade de Lisboa, Instituto Superior Técnico (2022).
- [54] M. Pozar, *Microwave Engineering*, 4th Edition, Wiley, 2012.

Appendix

A. Signal injection

In a mono-static system, the signal is injected and detected in the same fundamental waveguide. The waveguide cross-section is assumed to be rectangular since most of the antennas use this geometry and the fundamental mode expression is simpler to implement. Other geometries can be excited adapting the code. The dimensions of the source are determined by the number of points on each side of the rectangular waveguide. The field is excited in a y - z plane defined by i_{src} (x direction) and by a minimum and maximum j (y direction) and k (z direction) index values, $[j_{min}, j_{max}]$ and $[k_{min}, k_{max}]$ respectively. By definition, the first and last point of the source is located at the metallic structure, where the field value is zero. If the magnetic field is aligned with the z direction, the TE mode corresponds to O-mode reflectometry and the TM mode to the X mode.

Before exciting the mode, the mirror necessary for the UTS is implemented before the source position. The impulsive response of the system is then evaluated during n_{UTS} iterations. In the 2D simulations, the values associated with each field are saved in memory in a 2D matrix with $n_{UTS} \times l_{src_y}$ elements. And in the 3D simulations, in a matrix with $n_{UTS} \times l_{src_y} \times l_{src_z}$ elements. The TM mode is excited with the E_z component of the electric field in the form [54]:

$$E_z(i_{src}, j, k) = \sin \left[\frac{m\pi}{(j_{max} - j_{min})} (j - j_{min}) \right] \sin \left[\frac{n\pi}{(k_{max} - k_{min})} (k - k_{min}) \right], \quad (97)$$

where m and n are the mode indices, $j_{min} \leq j \leq j_{max}$ and $k_{min} \leq k \leq k_{max}$. The source amplitude is 1 V/m, by default. The relative detected amplitude has the same value as the absolute one. The TE mode expression is excited with the H_z field which has a similar form. The source length in the y and z direction (l_{wg_y} and l_{wg_z}) is:

$$[l_{wg_y}, l_{wg_z}] = [j_{max} - j_{min} + 1, k_{max} - k_{min} + 1]. \quad (98)$$

In REFMUL* codes, the source lengths are chosen to have odd values. This choice is preferable from a numerical standpoint due to symmetry considerations and allows for probing the amplitude of the electric field at the central position, ensuring that it reaches its maximum value. Consequently, it is recommended to describe the source using the center positions j_{src} and k_{src} , along with the half-widths of the waveguide, h_{wg_y} and h_{wg_z} . The relation with the minimum and maximum indices of the waveguide is

$$[j_{src}, h_{wg_y}] = [j_{min} + h_{wg_y}, (l_{wg_y} - 1)/2], \quad (99)$$

$$[k_{src}, h_{wg_z}] = [k_{min} + h_{wg_z}, (l_{wg_z} - 1)/2]. \quad (100)$$

In two dimensions, the designation is the same, but the excitation is done in one line. In one dimension, it is done in one point and there is no metallic structure. The time dependence of the signal for FMCW (Frequency Modulated Continuous Wave) reflectometry can be divided into five phases, each with different phase and amplitude behaviors. In the first phase (T_{s1}) the amplitude of the signal increases to 1 with an hyperbolic tangent frame. The frequency is the minimum frequency of the range, f_{min} . In the second phase (T_{s2}), the frequency is the same but the amplitude is constant. In the third phase, (T_{s3}), the frequency is swept from f_{min} to f_{max} . In the fourth phase (T_{s4}), the amplitude is constant but the frequency is constant at f_{max} . In the last phase, the frequency is the same but the amplitude decreases with an hyperbolic tangent frame. The size of each phase is determined by the correspondent number of time iterations. In REFMUL* these times are defined by five variables,

$$[n_{rise}, n_{fall}, n_{pre}, n_{pos}] = [T_{s1}, T_{s5}, T_{s1} + T_{s2}, T_{s4} + T_{s5}] / \Delta t, \quad (101)$$

$$n_{ramp} = (T_{s1} + T_{s2} + T_{s3} + T_{s4} + T_{s5}) / \Delta t. \quad (102)$$

The band frequencies are between the first and the second cutoff frequencies of the waveguide,

$$f_1 < f_{min} < f_{max} < f_2, \quad (103)$$

where f_1 and f_2 are the cutoff frequencies of the first and second mode that is intended to propagate and f_{min} and f_{max} the initial and final band frequencies. However, the waveguide dimensions are discretised. Even though the

continuous waveguide is fundamental for the considered band, it may not be when it is converted to the FDTD grid. The design of the fundamental waveguide involves finding f_1 and f_2 for different discrete values of h_{wgy} and h_{wgz} (1, 2, ...) and finding a combination that respects the maximum bandwidth imposed by condition 103. This process can be illustrated with the example of the 2D TM mode. The first two cutoff frequencies of a 2D waveguide with width $a = 2h_{wg}\Delta x$ are

$$f_1 = \frac{f_2}{2} = \frac{c}{2a} = \frac{N_\lambda f_0}{4} \frac{1}{h_{wg}}. \quad (104)$$

This implies a maximum value of the bandwidth $\Delta f|_{max}$ admitted by the grid of

$$\Delta f|_{max} = f_2 - f_1 = \frac{N_\lambda f_0}{4} \frac{1}{h_{wg}}. \quad (105)$$

In the ideal case, the frequency bands and the fundamental waveguides correspond to the real ones. The simulation of a measurement process requires simulations for different bands, changing the fundamental waveguide in each one. When the real bandwidths are not compatible with the grid, they need to be divided in different virtual bands. This introduces an error associated with the new fundamental waveguides. In some cases the real waveguides support the band but the discrete versions do not.

B. Signal detection

With the UTS implemented, the detection point at a mono-static reflectometer can be done at

$$r_{det} = (i_{det}, j_{det}, k_{det}) = (i_{src}, j_{src}, k_{src}) - (1, 0, 0). \quad (106)$$

The figure 20 shows a zoom at the source region with the wall removed where is possible to identify the points of the metallic structure, the source point r_{src} , the detection location r_{det} and the half width of the waveguide h_{wg} .

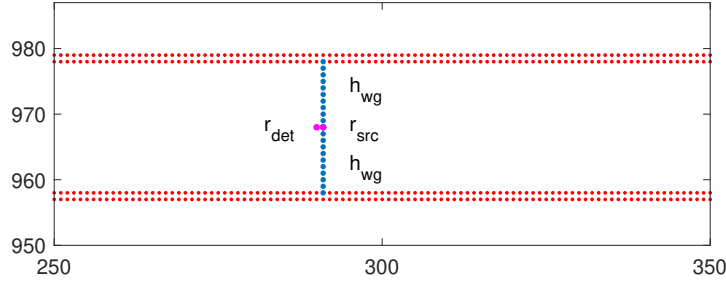


Fig. 20: Zoom at the fundamental waveguide model.

The signal coming from the plasma is usually adapted to the fundamental waveguide using a taper, which is also used to match the fundamental mode to the antenna waveguide. One issue that arises in detection is that the signal from the plasma can excite high-order modes at the start of the fundamental waveguide. Therefore, the detection point must be positioned where the attenuation of these modes is high compared to the fundamental mode. In the case of the rectangular waveguide, the β propagation constant is

$$\beta = \sqrt{\left(\frac{2\pi f}{c}\right)^2 - \left(\frac{m\pi}{a}\right)^2 - \left(\frac{n\pi}{b}\right)^2} = j\sqrt{\left(\frac{m\pi}{a}\right)^2 + \left(\frac{n\pi}{b}\right)^2 - \left(\frac{2\pi f}{c}\right)^2} \quad (107)$$

for a decaying mode. Higher order modes decay faster. Therefore the condition for detection is

$$A_2(i_{det}, j_{det}, k_{det}) = A_2(i_{iwg}, j_{det}, k_{det})e^{j\beta_2 d_{det}} \ll A_1(i_{det}, j_{det}, k_{det}), \quad (108)$$

where i_{iwg} is the position of the waveguide interface with the taper, A_2 is the second mode amplitude, A_1 the amplitude of the fundamental mode, β_2 the amplitude decaying constant of the second order mode, and d_{det} the distance that the

detection should be placed from the fundamental waveguide-taper interface. The source position can be placed at the same location according to equation (106), simplifying the analysis of the detected signals.

By normalizing the excited field inside the fundamental waveguide, it becomes possible to determine whether only the fundamental mode is being detected. In the TM mode case, if the electric field is normalized by

$$\mathbf{E}^N(x, y) = \frac{\text{abs}[\mathbf{E}(x, y)]}{\text{max}[\text{abs}[\mathbf{E}(x, y)]]_{\text{src}}}, \quad (109)$$

it is possible to determine if the mode is purely fundamental at the detection position by examining if the contour plot inside
value i
GHz f

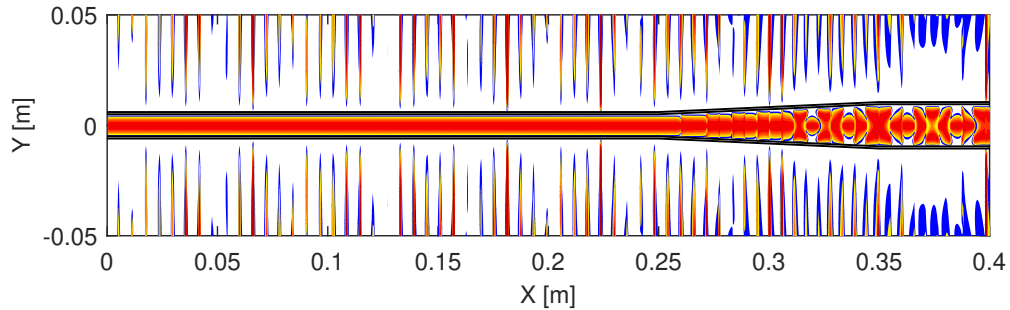


Fig. 21: The normalized electromagnetic field at 28 GHz.

The presence of straight contour lines observed 10 cm before the taper confirms that only the fundamental mode is being measured. The taper effectively rejects other modes, resulting in the modulation of the normalized electric field, which represents a superposition of the inward and outward waves.

C. Baseline scenario density map

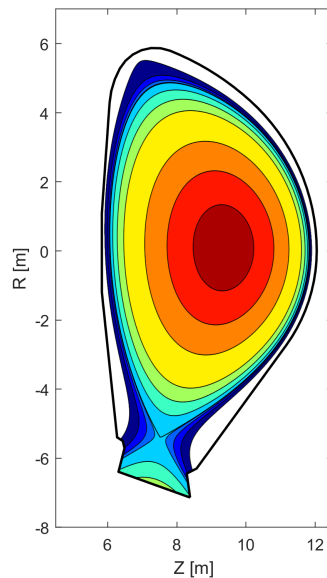


Fig. 22: Density map (poloidal cross-section) obtained with the 2017 baseline scenario.

D. Simulated models

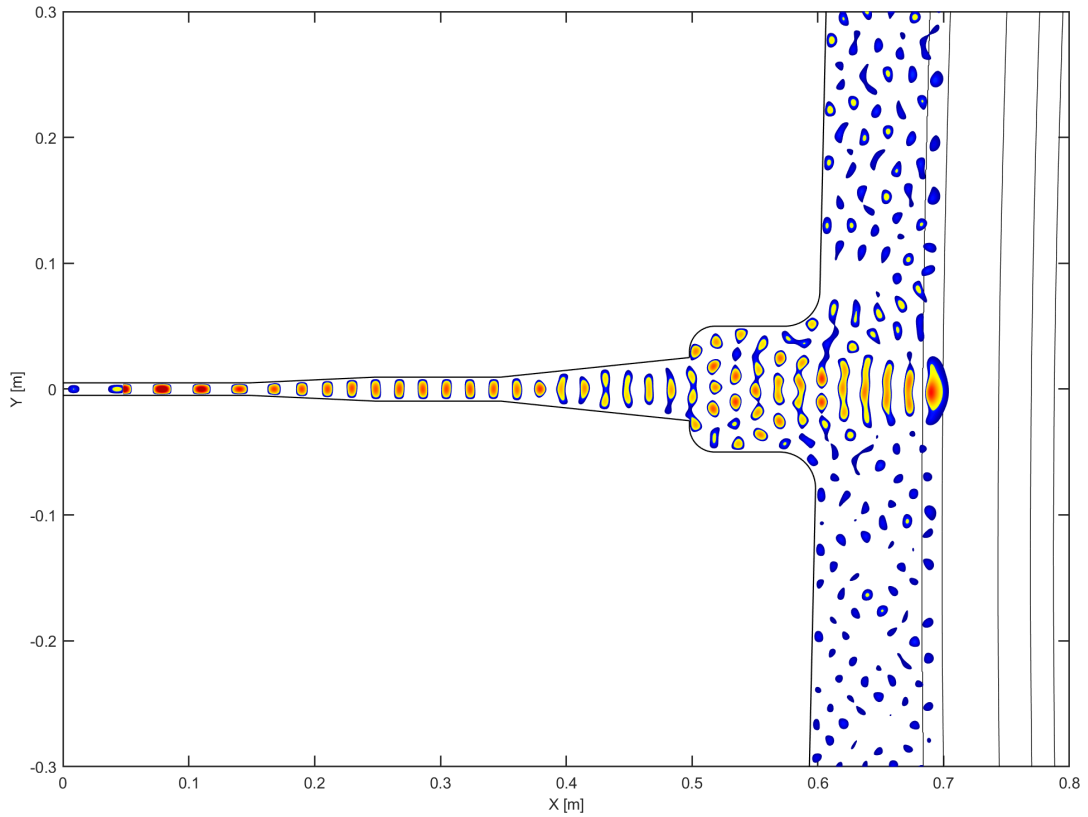
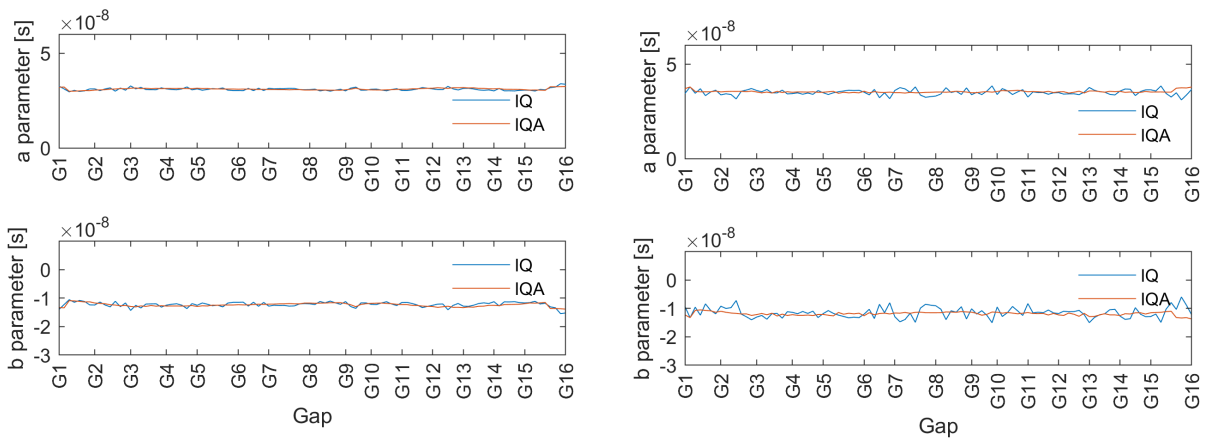


Fig. 23: Snapshot of the positive part of the electric field at 40 GHz for the gap 13 with the cavity setup.

E. Fit parameters of the waveguide propagation function



(a) Comparison of the fit parameters of the waveguide propagation function for the antenna with the wall removed.

(b) The fit parameters of the waveguide propagation function for the cavity setup.

Fig. 24: The fit parameters of the waveguide propagation function for the cavity setup.